

Journal of Astronomical Telescopes, Instruments, and Systems

AstronomicalTelescopes.SPIEDigitalLibrary.org

Replacing the polarizer wheel with a polarization camera to increase the temporal resolution and reduce the overall complexity of a solar coronagraph

Nelson L. Reginald
Natchimuthuk Gopalswamy
Seiji Yashiro
Qian Gong
Madhulika Guhathakurta

SPIE.

Nelson L. Reginald, Natchimuthuk Gopalswamy, Seiji Yashiro, Qian Gong, Madhulika Guhathakurta, "Replacing the polarizer wheel with a polarization camera to increase the temporal resolution and reduce the overall complexity of a solar coronagraph," *J. Astron. Telesc. Instrum. Syst.* **3**(1), 014001 (2017), doi: 10.1117/1.JATIS.3.1.014001.

Replacing the polarizer wheel with a polarization camera to increase the temporal resolution and reduce the overall complexity of a solar coronagraph

Nelson L. Reginald,^{a,b,*} Natchimuthuk Gopalswamy,^b Seiji Yashiro,^{a,b} Qian Gong,^c and Madhulika Guhathakurta^d

^aThe Catholic University of America, Department of Physics, Washington, District of Columbia, United States

^bNASA-Goddard Space Flight Center, Solar Physics Division, Greenbelt, Maryland, United States

^cNASA-Goddard Space Flight Center, Optical Science Division, Greenbelt, Maryland, United States

^dNASA HQ, Heliophysics Science Division, Washington, District of Columbia, United States

Abstract. Experiments that require linearly polarized brightness measurements, traditionally have obtained three successive images through a linear polarizer that is rotated through three well-defined angles and the images are combined to get the linearly polarized brightness. This technique requires a mechanism to hold the linear polarizer in place and to precisely turn it through the three angles. Obviously, the temporal resolution is lost in such a scenario, since the three images that are used to derive the linearly polarized brightness are taken at three different times. Specifically, in a dynamic corona that is in constant reshaping of its structures, the linearly polarized brightness image produced in this manner may not yield true values all around the corona. In this regard, with the advent of the polarization camera, the linearly polarized brightness can be measured from a single image. This also eliminates the need for a linear polarizer and the associated rotator mechanisms and can contribute toward lower weight, size, power requirements, overall risk of the instrument, and most importantly, increase the temporal resolution. We evaluate the capabilities of a selected polarization camera and how these capabilities could be tested in a ground experiment conducted in conjunction with a total solar eclipse. The ground experiment requires the measurement of the linearly polarized brightness, also known as K-corona, in a corona that also contains unpolarized brightness, known as F-corona, in order to measure three important physical properties pertaining to coronal electrons, namely, the electron density, electron temperature, and the electron speed. © The Authors. Published by SPIE under a Creative Commons Attribution 3.0 Unported License. Distribution or reproduction of this work in whole or in part requires full attribution of the original publication, including its DOI. [DOI: [10.1117/1.JATIS.3.1.014001](https://doi.org/10.1117/1.JATIS.3.1.014001)]

Keywords: solar corona; linearly polarized brightness; linear polarizer; polarization camera.

Paper 16026 received May 6, 2016; accepted for publication Jan. 9, 2017; published online Feb. 7, 2017.

1 Introduction

The solar corona continues to intrigue with its million-degree (K) temperature, which is much higher than the sun's surface temperature of ~ 6000 K. The corona is also the birth place of flows such as the solar wind and transient events such as coronal mass ejections (see Ref. 1). With the coronal matter in a highly ionized state, it is very important to generate routine information on the physical properties, such as coronal temperatures and flow speeds of both the ions and electrons to understand the coronal dynamics and unravel its mysteries.

The solar coronal brightness observed during a total solar eclipse is due to the photospheric light scattered off both the electrons and ions in the solar corona. The photospheric radiation scattered off the electrons, which is commonly known as Thomson scattering, is linearly polarized and is called the K-corona, while the photospheric radiation scattered off everything else in the corona is unpolarized and is called the F-corona. Therefore, the simplest technique to differentiate between the K and F coronal brightness is to take three images through the use of a linear polarizer that needs to be turned precisely through three well-defined angles as explained in Ref. 2. In another

example, with the coronagraph-1 (COR1) instrument on board the Solar Terrestrial Relations Observatory (STEREO) spacecraft (see Ref. 3), the linearly polarized brightness is measured by rotating the linear polarizer through three well-defined angles at 120 deg apart. This technique requires a mechanism to hold the linear polarizer in place and to precisely turn it through the three angles. Obviously, the temporal resolution is lost in such a scenario, since the three images that are used to derive the linearly polarized brightness are taken at three different times. Specifically, in a dynamic corona that is in constant reshaping of its structures, the linearly polarized brightness image produced in this manner may not yield true values all around the corona. However, with the advent of the polarization camera, the linearly polarized brightness can be measured from a single image, although this is not the only method for ellipsometry using a single exposure. This will also eliminate the need for a linear polarizer and the associated rotator mechanisms and can contribute toward lower weight, size, power requirements, overall risk of the instrument, and most importantly, increase the temporal resolution. The field-of-view of the COR1 instrument is 1.3 to 5 R_{\odot} , which is within the region where the K and F are totally linearly polarized and totally unpolarized, respectively.

One such effort in using the coronal electrons to map the coronal temperature and speed in the solar corona is the use of the Imaging Spectrograph of Coronal Electrons (ISCORE)

*Address all correspondence to: Nelson L. Reginald, E-mail: Nelson.L.Reginald@nasa.gov

instrument described in Ref. 4. In the ISCORE instrumental concept, the electron temperature and flow speed are measured by taking four consecutive coronal images of the solar corona using a linear polarizer with a mechanism to turn through three well-defined angles for each of four filters centered at 385.0, 398.7, 410.0, and 423.3 nm with a bandpass of ~ 5 nm. The details are explained by Reginald and Davila⁵ and Reginald et al.⁶ Here, the coronal images through (385.0 and 410.0 nm) filters and (398.7 and 423.3 nm) filters will measure the electron temperature and speed, respectively.

In past experiments using the ISCORE instruments in conjunction with total solar eclipses, we were restricted to employing just two filters that measured only the electron temperature, restricting our observations to coronal heights below $1.5 R_{\odot}$ from the sun center and also not deploying a linear polarizer for the following two reasons. First, for this experiment to succeed, we need a noise-to-signal ratio of $<1\%$ in order to measure the temperature and speed within ± 0.2 MK and ± 200 km s⁻¹ MK, respectively. As a result, repeat measurements through each filter are needed to satisfy this requirement. Second, the short durations of total solar eclipses severely limit the number of exposures that can be made during totality and even deprives us of time needed to turn a linear polarizer through three well-defined angles for each image. As a consequence, we had to restrict our observations to low solar coronal heights of $1.5 R_{\odot}$ from the sun center. In this region, the coronal images taken without a linear polarizer or total brightness images will still contain both K and F brightness components. However, from Fig. 1, from Phillips,⁷ that shows the K and F brightness profiles measured from the sun center to the earth's orbit in solar radii, it is evident that the K component overwhelms the F component by orders of magnitude at coronal heights below $1.5 R_{\odot}$ from the sun center. Therefore, the ISCORE experimental results from Reginald et al.⁴ that did not use a linear polarizer but restricted its observations to coronal heights below $1.5 R_{\odot}$ from the sun center are reasonable.

The only viable alternate option to overcome the limitations of the ISCORE instrument for deployment during a total solar eclipse is to use a polarization camera that is capable of simultaneously measuring the total brightness (K+F), linearly polarized brightness (K), and unpolarized brightness (F) in every single image, which will eliminate the need to turn a linear polarizer through three angles for each of the four filters, which allows us to use all four filters to measure both electron temperature and speed, and also allows us to observe up to a coronal height of $4 R_{\odot}$ from the sun center.

Here, we wish to emphasize that even with linearly polarized brightness measurements, our measurement is restricted to areas below coronal height of $4 R_{\odot}$ from the sun center. This is because the F component that is caused by diffraction and reflection off solid dust particles along the line-of-sight is also polarized by an unpredictable amount based on the nature of the dust particles. Although closer to the solar limb, the F component is mainly due to diffraction off the dust particles and is totally unpolarized, the F component will begin to become partially polarized beyond $\sim(4-5) R_{\odot}$, as shown by Mann,⁸ while the K component will always be totally linearly polarized. As a result, beyond $\sim(4-5) R_{\odot}$ from the sun center, it would not be feasible to totally isolate the F and K components using polarization techniques.

To test the potential of the polarization camera, the ISCORE instrument described by Reginald et al.⁴ was reconfigured to

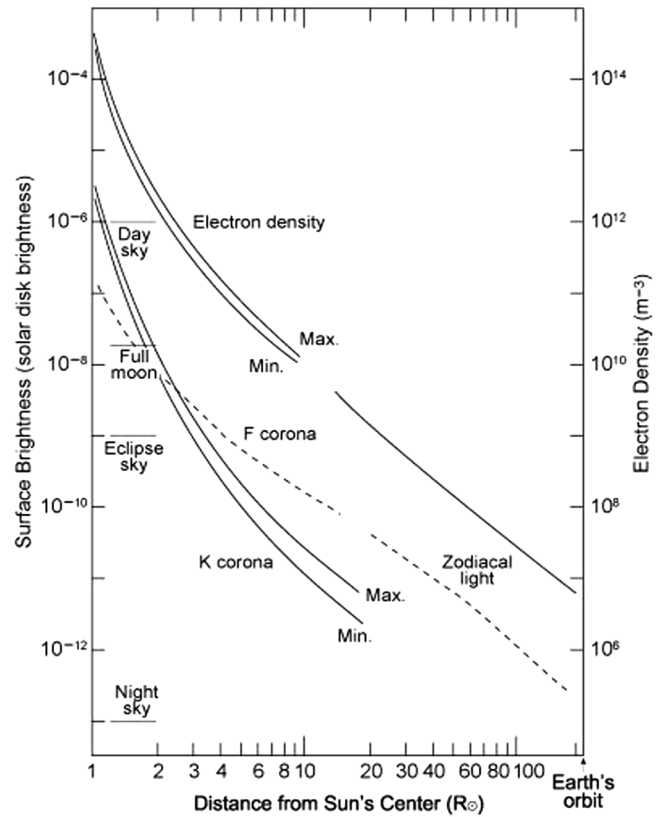


Fig. 1 A plot showing the K and F coronal brightness scaled to the solar disk brightness (left scale) and electron density (right scale) versus the distance from the sun center in solar radii. Also shown for comparison purpose are the surface brightness for the full moon and clear sky for day and night and during total solar eclipses. The maximum and minimum of the solar magnetic activity cycle are designated by “max” and “min.” The F component begins to exceed the K component around $3 R_{\odot}$ (see Fig. 5.1 in Phillips⁷).

accommodate a polarization camera together with a filter wheel that housed four filters centered at 385.0, 398.7, 410.0, and 423.3 nm to measure both the electron temperature and speed in conjunction with the total solar eclipse of March 9, 2016, in Maba, Indonesia. Unfortunately, we were clouded out. Nevertheless, we plan on testing the ISCORE instrument in this new configuration during the total solar eclipse of August 21, 2017, in the United States.

Here, we describe polarization measurements achieved by modulating the intensity of the radiation based on the state of polarization of an incoming beam. The modulation techniques can be categorized into three domains, namely, temporal, spatial, and spectral. In the temporal modulation, the polarization parameters are measured sequentially in time by rotating a retarder or a linear polarizer; in the spatial domain, the polarization parameters are measured simultaneously by splitting the incoming beam; and in the spectral modulation, one or more sinusoidal patterns are superimposed on the incoming beam. The ISCORE instrument with the micropolarizer array placed in front of the detector in the focal plane can be categorized as a division of focal plane polarimetry in the spatial domain and examples of other types of divisions, such as division of amplitude, time amplitude, and aperture polarimetry, and the domains to which they belong, are described in detail in Fig. 1 by Vorobiev and Ninkov.⁹ A fundamental problem

associated with this category is that the four pixels that constitute the super pixel to derive the polarization parameters do not see the same area on the object that is being imaged. This will be a problem if the four areas from the object that are seen by the four pixels differ much in brightness and polarization. However, in the case of the low solar corona imaged by the ISCORE instrument in the current configuration, each pixel will image an area $0.004 R_{\odot} \times 0.004 R_{\odot}$ of the object plane, which is the solar corona and will not cause a significant impact except in localized areas that are subject to coronal brightening.

2 Description of the Polarization Camera

There are many polarization cameras in the market and here we describe in detail the polarization camera that we plan to use with the ISCORE instrument. The polarization camera known as the ‘‘PolarCam’’ is from 4-D Technology Corporation, Arizona, United States, and is described in detail by Brock et al.¹⁰ The 4D Technology Corporation incorporates a micropolarizer array on to a charge-coupled device (CCD) by Kodak. The micropolarizer array contains a pattern of linear polarizers with four discrete polarizations at angles 0, 45, 90, and 135 deg, as shown in Fig. 2, which is known as a super pixel and is repeated over the entire array. Therefore, in the final image, the brightness arrays for each of the above four polarization angles will be one-fourth the size of the original array, and these four arrays will measure the linear polarization intensities at 0, 45, 90, and 135 deg angles of polarization, which we will call I_0 , I_{45} , I_{90} , and I_{135} , respectively. The camera containing the CCD is from Imperx, Inc., Florida, United States, and is known as an Imperx Bobcat camera. The CCD in this camera is a monochrome CCD of size 2048×2048 pixels (clear area 1976×1980 pixels) with each pixel having dimensions $7.4 \mu\text{m} \times 7.4 \mu\text{m}$. The camera electronics allow for a maximum frame grab rate of 16 frames/s at any of the allowed bit depths of 8, 12, and 16. The minimum and the maximum exposure periods are $10 \mu\text{s}$ and 16 s, respectively. The spectral response of the CCD extends from 300 to 1000 nm with quantum efficiencies of 0.25 at 350 nm and 0.45 at 450 nm, which amply serves our purpose.

When the above pixelated polarization camera is used as an imaging polarimeter, the source is imaged directly on to the polarization array (PA). The data related to each super pixel

shown in Fig. 2 can be expressed using Eq. (1) to determine the Stokes vector (S) pertaining to that super pixel in terms of the counts registered by the camera from the four pixels constituting that super pixel. In Eq. (1), the quantities I_0 , I_{45} , I_{90} , and I_{135} are the intensities of the linear polarization components at 0, 45, 90, and 135 deg, respectively, and the I_{LHC} and I_{RHC} are the left and right circular polarization components, respectively. However, in the micropolarizer array pertaining to this camera that contains only linear polarizers embedded into each pixel according to the pattern shown in Fig. 2, we can determine only S_0 , S_1 , and S_2 components of the Stokes vector. In order to determine S_3 , we would need additional optical components such as a waveplate introduced into the camera, which will definitely compromise the simplicity and the instantaneous imaging capability of the camera. This inadequacy does not serve as a limitation in our work because the source we plan to image is linearly polarized as elaborated below.

In solar astronomy, we always assume S_3 to be zero in the visible light region of the solar corona although it is not true in the infrared, microwave regions, and beyond. This assumption is based on the fact that the F and K coronal brightenings that brighten the solar corona are completely unpolarized and completely linearly polarized, respectively, at least up to a coronal height of $4 R_{\odot}$ from the sun center. For example, space-based solar coronagraphs, such as the coronagraph instruments C1, C2, and C3 on-board the Solar and Heliospheric Observatory (SOHO) spacecraft and the coronagraph instruments COR 1 and COR 2 on-board the STEREO spacecraft that measure the K-coronal brightness, are only equipped with a linear polarizer mounted on a motorized wheel to enable taking three images by rotating the linear polarizer through intervals of 120 deg to determine the linearly polarized brightness that pertains to the K-corona. Similarly, ground-based coronagraph, such as MK4 at Mauna Loa Solar Observatory (MLSO), Hawaii, measures the linearly polarized brightness of the solar corona by turning a linear polarizer through three angles at intervals of 120 deg. As such, in the context of the ISCORE instrument that operates in the visible light region and functions like a solar coronagraph that uses the moon to occult the sun, the term polarized brightness will always mean linearly polarized brightness and S_3 will always be zero and will reflect this fact in Eq. (1) and all subsequent equations:

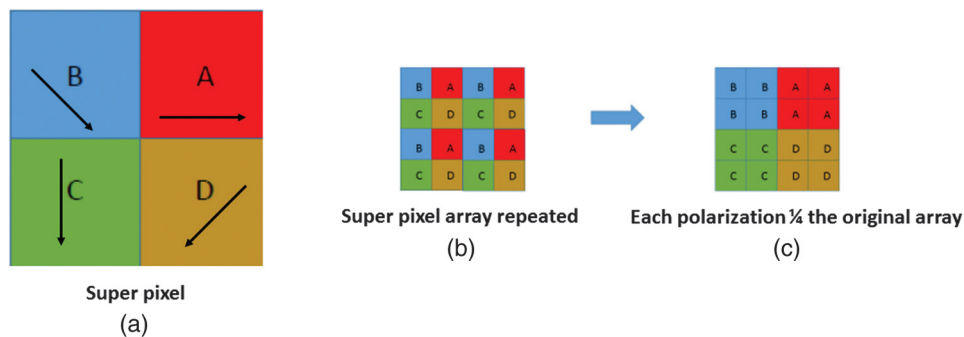


Fig. 2 Schematic diagram of the polarization camera CCD array. Each super pixel (a) comprises of four pixels with micropolarizer array of four discrete polarizations of angles 0, 45, 90, and 135 deg embedded on the four pixels labeled as A, B, C, and D, respectively. (b) This pattern is then repeated over the entire array on the CCD of size 2048×2048 pixels (clear area 1976×1980 pixels). (c) For each image taken by the camera, the intensities I_0 , I_{45} , I_{90} , and I_{135} pertaining to the four angles of polarization will then be one out of four quadrants of the original array size with dimensions 988×990 pixels ($1976/2 \times 1980/2$) for a total of 978,120 pixels.

$$S = \begin{pmatrix} S_0 \\ S_1 \\ S_2 \\ S_3 \end{pmatrix} = \begin{pmatrix} I_0 + I_{90} \\ I_0 - I_{90} \\ I_{45} - I_{135} \\ I_{\text{LHC}} - I_{\text{RHC}} \end{pmatrix}. \quad (1)$$

Equation (2) shows the relation among the total brightness (tB), the degree of linear polarization (DOLP), the linearly polarized brightness (pB), and the angle of linear polarization (AOLP) of the incident light relative to the detector axis and the Stokes vectors S_0 , S_1 , S_2 , and S_3 :

$$\begin{aligned} \text{tB} &= S_0, \\ \text{DOLP} &= \frac{\sqrt{(S_1^2 + S_2^2)}}{S_0}, \\ \text{pB} &= \sqrt{(S_1^2 + S_2^2)}, \\ \text{AOLP} &= \frac{1}{2} \times \arctan\left(\frac{S_2}{S_1}\right). \end{aligned} \quad (2)$$

Our next step is to derive, from first principles, the relation among the Stokes vectors S_0 , S_1 , S_2 , and S_3 and the measured intensities I_0 , I_{45} , I_{90} , and I_{135} in Eq. (1) in a super pixel. The four orientations of the four linear polarizers embedded in the four pixels in a super pixel are equivalent to rotating a linear polarizer through the four angles in a beam containing unpolarized and linearly polarized light. Then applying the Malus law for the four orientations of the linear polarizer, we obtain Eq. (3), where I_t , I_p , I_u , and θ are the total intensity, linearly polarized intensity and unpolarized intensity and angle between the plane of polarization and the reference direction, respectively, of the beam:

$$\begin{aligned} I_0 &= \frac{I_u}{2} + I_p \times \cos^2(\theta), \\ I_{45} &= \frac{I_u}{2} + I_p \times \cos^2(45 - \theta), \\ I_{90} &= \frac{I_u}{2} + I_p \times \cos^2(90 - \theta), \\ I_{135} &= \frac{I_u}{2} + I_p \times \cos^2(135 - \theta). \end{aligned} \quad (3)$$

Then, from Eq. (3), after some manipulation, we can obtain the following expressions for I_t (or tB), I_p (or pB), and I_u (or uB), as shown in Eq. (4) (see Ref. 2). Since the pixelated array includes two sets of orthogonal polarizations, we can measure tB from two different ways and use the redundant data to check for accuracy and use it to minimize noise in the measurements:

$$\begin{aligned} \text{tB} &= I_0 + I_{90} = I_{45} + I_{135} = \frac{(I_0 + I_{45} + I_{90} + I_{135})}{2} = S_0, \\ \text{pB} &= \sqrt{[(I_0 - I_{90})^2 + (I_{45} - I_{135})^2]} = \sqrt{(S_1^2 + S_2^2)}, \\ \text{uB} &= \text{tB} - \text{pB}. \end{aligned} \quad (4)$$

In the context of the solar corona, tB, pB, and uB in Eq. (4) can be related to total brightness (K+F), linearly polarized brightness (K), and unpolarized brightness (F) of the corona, respectively.

3 Characterization of the Polarization Camera

In this section, we first define and consider three noise generation processes that can affect the digital counts recorded by each pixel in the CCD. Then we show how these three noise levels can be quantified through tests to determine the margins of error associated with these three noise levels on the actual digital counts recorded by each pixel of the raw images captured by the CCD. The three noise generation processes in the CCD that will be considered are the dark noise (σ_{dark}) generation from dark current, statistical noise ($\sigma_{\text{statistical}}$) generation from counting the incident photons on the CCD, and read noise (σ_{read}) generation from analog-to-digital conversion process in the CCD. Here, we wish to state that these three noise levels have to be determined for each raw image recorded by the CCD to determine associated random error (σ_{random}), which is given by $\sqrt{(\sigma_{\text{dark}}^2 + \sigma_{\text{statistical}}^2 + \sigma_{\text{read}}^2)}$. Then we consider the pixel sensitivity variations from pixel-to-pixel in the CCD and the methodology employed to correct for this sensitivity variations through flat fielding. Finally, we study in detail to quantify the systematic error ($\sigma_{\text{systematic}}$) associated with the micropolarizer array embedded on the CCD, which makes this camera a polarization camera. We acknowledge there are other sources of error in addition to the ones listed above, but in this paper, we will only focus on the errors listed above. Basically, random error can be minimized by averaging over a large number of observations while systematic error requires carefully spotting and then correcting the error. We will also confirm through laboratory experiments some unique characteristics of the polarization camera and also address the issue of instrumental polarization.

3.1 Random Error

First, we consider the dark noise (σ_{dark}) generation in the polarization camera. The dark current is the technical term that defines the generation of electrons within the CCD even without absorption of photons. The magnitude of the dark current is closely associated with the operating temperature of the CCD and exposure durations. The magnitude of the dark current can be minimized by lowering the operating temperature of the CCD using a thermoelectric cooler although this feature is not available in the polarization camera described in this paper. Also, it is important to note that the CCD will not generate the same level of dark current in equivalent periods of time and this phenomenon gives rise to a dark noise. If not for the dark noise, the digital counts associated with the dark current can be easily removed from the raw image by subtracting a dark image taken with the camera shutter closed and with an exposure time matching the raw image. However, the dark noise, meaning the fluctuations in the amount of dark current for equivalent periods of time, has to be quantified to determine its contribution toward the error margins in the digital counts registered by the CCD. To quantify the dark noise, we followed the following steps. We took 10 dark images for durations of 1 to 12 s in 1-s interval. Then using the 10 dark images for each duration of exposure, the average dark counts over 978,120 pixels (988 × 990 pixels) for each of the four polarization states on the CCD were calculated. For example, Table 1 shows the average dark counts registered by 978,120 pixels in 10 images of 1 s of exposure in each of the four states of polarization on the CCD. The four states of polarization are named P000, P045, P090, and P135 in the columns and the rows marked 1 to 10 represent the average counts

Table 1 Average dark counts registered by 10 frames of 1 s exposure by 978,120 pixels that represent each of the four states of the polarization in the CCD. The four states of polarization are named P000, P045, P090, and P135 in the columns and the 10 different exposure frames are listed along the rows. Similar tables were created for exposures lasting 1 to 12 s in 1-s interval with the camera shutter closed.

Pol. state/frame number	P000	P045	P090	P135
1	424.5	434.5	434.2	424.5
2	424.2	438.5	439.4	426.6
3	422.2	440.2	437.5	422.5
4	413.1	430.4	430.9	413.5
5	436.3	421.7	420.2	433.9
6	437.2	419.2	420.5	438.1
7	428.0	410.7	412.5	429.0
8	412.3	432.1	431.9	411.7
9	427.5	407.7	409.9	427.7
10	402.2	426.0	425.2	403.5
Mean (frames 1 to 10)	422.9	426.1	426.2	423.1
Standard deviation	± 10.9	± 11.2	± 10.2	± 10.7

registered by all the pixels in each state of polarization in the 10 sample dark images. In each column, it is apparent that the average dark counts over the 10 frames fluctuate for all four states of polarization. The penultimate row in Table 1 shows the mean of the average dark counts from the 10 images for each of the polarization states and the last row shows the standard deviation of the mean, which is used as a measure of the dark noise for that polarization state. Data pertaining to Table 1 were created for additional exposure times that lasted 2 to 12 s in intervals of 1 s and Table 2 shows the standard deviation or the dark noise determined for each of the other exposure time periods.

In Fig. 3, we have plotted the data from Table 2 against the related exposure times of the dark images for the four states of polarization. It is apparent from Fig. 3 that the dark noise counts fluctuate with exposure times in a sawtooth shaped pattern between dark noise counts levels of 10 and 45. It is also apparent that pixels in the CCD belonging to all four polarization states uniformly follow the same pattern showing a strong positive correlation and are confirmed by calculated linear Pearson correlation coefficients of 0.964, 0.964, and 0.999 to the pairs of data pertaining to (P000, P045), (P000, P090), (P000, P135), respectively. Here, we wish to note that the actual dark noise pertaining to subtracting a dark image from a raw image will be twice the dark noise derived from Fig. 3 for the corresponding exposure time. This accounts for the presence of dark noise in both the dark image used to remove the counts due to dark current as well as in the raw image.

Here, we wish to emphasize that in the real experiment, Tables 1 and 2 will be created for each individual pixel for a total of 1976×1980 (or 3,912,480) pixels. Here, just for brevity and demonstrating the technique employed to determine the

Table 2 Dark noise error (σ_{dark}) in terms of digital counts associated with the dark current measured by each of the four polarization states in the CCD. The four polarizations states composed of 978,120 pixels and are named P000, P045, P090, and P135 along the columns and the rows reflect the exposure times in seconds.

Pol. state/exposure time (s)	P000	P045	P090	P135
1	± 10.9	± 11.2	± 10.2	± 10.7
2	± 13.4	± 14.9	± 15.4	± 13.7
3	± 39.8	± 41.6	± 41.6	± 39.8
4	± 38.9	± 43.7	± 44.5	± 38.6
5	± 20.8	± 22.1	± 21.8	± 20.9
6	± 38.1	± 40.9	± 41.5	± 38.4
7	± 23.0	± 24.6	± 25.1	± 23.4
8	± 41.4	± 40.1	± 40.4	± 40.8
9	± 27.8	± 32.3	± 32.5	± 27.9
10	± 37.7	± 31.8	± 32.2	± 38.1
11	± 42.6	± 40.1	± 40.0	± 43.5
12	± 33.0	± 32.4	± 32.7	± 33.4

dark noise, the averages for all the pixels in each polarization state, comprising 978,120 pixels for each polarization state, were computed to create Tables 1 and 2. It is true that measuring the dark noise using the averages could be susceptible to bad pixels and illumination from cosmic rays and a measurement

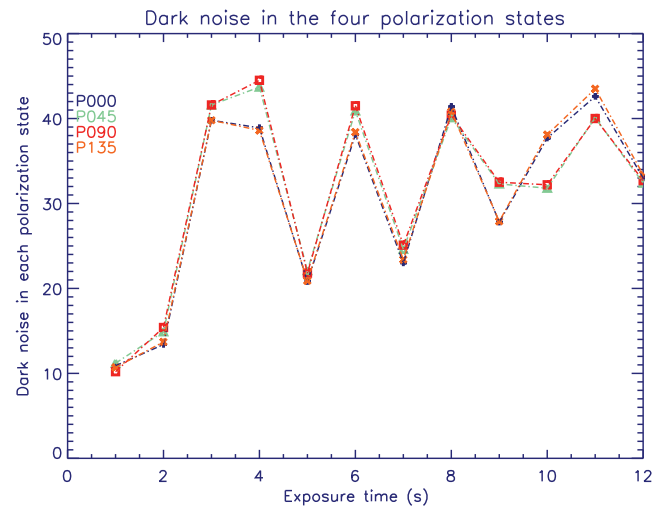


Fig. 3 Plot of standard deviation values (or dark noise counts) from Table 2 against the related exposure times determined from the dark images for the four states of polarization. We also see that the dark noise counts fluctuate with exposure times in a sawtooth shaped pattern between dark noise counts levels of 10 and 45. The calculated linear Pearson correlation coefficients for pairs of data pertaining to (P000, P045), (P000, P090), and (P000, P135) are 0.964, 0.964, and 0.999, respectively.

based on medians would be a better measure of the dark noise. From past experience, we see that the illumination of CCD pixels by cosmic rays is a rarity in laboratory or ground-based experiments although prevalent in space-based experiments. Since these averages would be determined through dark images on each individual pixel, we can easily observe any anomalies and exclude those individual pixels from analysis. Now, to quantify σ_{dark} as percentage of the measured digital counts, suppose we calibrate the exposure times so that pixels fill up to half the full well depth of 32,768 counts [at 16-bit digitization the full well depth is (2^{16}) or 65,536 digital counts] for the raw images and assume σ_{dark} to be twice the maximum from Fig. 3 or 90 digital counts accounting for σ_{dark} present in both the raw and dark images will yield a measurement error $90/32,768$ or $\pm 0.27\%$ of the measured digital counts. In order to minimize σ_{dark} , the measured digital counts of the raw images can be maximized through longer exposure times or repeated measurements.

Second, we consider the statistical noise ($\sigma_{\text{statistical}}$) generation in the polarization camera. The statistical noise, also known as photon noise, results from the inherent statistical variation in the arrival rate of incident photons on to the CCD. The registered signal by the CCD is from converting photons to photoelectrons within the CCD. However, the magnitude of this registered signal is perturbed by the incident photons and follows a Poisson statistical distribution. The associated statistical error is then a function of the square root of the actual electrons that contribute toward the measured digital counts and is calculated in the following manner. For a CCD with 16-bit digitization and a full well depth of 300,000 electrons per pixel, the maximum digital counts that a pixel can register is 65,536 (2^{16}), which means 4.57 electrons generate 1 digital count. For example, for a pixel with 400 measured digital counts, the number of electrons required to generate 400 digital counts would be 1828 (400×4.57), which in turn generates a statistical noise level of 42.76 ($\sqrt{1828}$) electrons and corresponds to 9.36 ($42.76/4.57$) digital counts or 2.34% [$(9.36/400) \times 100\%$] of the measured digital counts. In our experiments, we like to calibrate our exposures times to generate at least half the maximum digital (or threshold for saturation) counts totaling 32,768 in a pixel or obtain this number by adding several raw images. Then, $\sigma_{\text{statistical}}$, as a percentage of the measured digital counts for a pixel at half its full well depth of 32,768 digital counts, as per the example above, would be ~ 85 digital counts or $\pm 0.26\%$ of the measured digital counts.

Third, we consider the read noise (σ_{read}) generation in the polarization camera that arises from reading an image from the CCD and converting in to a digital image file. σ_{read} was quantified to be 0.01 digital counts (or $0.01 \times 4.57 = 0.05$ electrons) by taking five zero exposure time dark frames (or 10 μs , which is the shortest integration time allowed by the software), also called bias frames, and then determining $\frac{\sigma[\text{average}(\text{biasframes}1-5)-\text{biasframe}1]}{\sqrt{2}}$. Then, σ_{read} , as percentage of the measured digital counts for a pixel with half the well depth of 32,768 counts, is insignificant.

Finally, the total random error (σ_{random}) due to σ_{dark} , $\sigma_{\text{statistical}}$, and σ_{read} for each pixel will be determined from the expression $\sqrt{(\sigma_{\text{dark}}^2 + \sigma_{\text{statistical}}^2 + \sigma_{\text{read}}^2)}$ (or 0.27%, 0.26%, insignificant) and measures to be $\pm 0.37\%$ of the measured digital counts for a pixel at half its full well depth and satisfies our requirement for σ_{random} to be $< 1\%$ of the measured digital counts. This is because when the noise-to-signal ratio is $\leq 1\%$, we can then

measure the temperature and speed within ± 0.2 MK and ± 200 km s $^{-1}$ MK, respectively, as explained by Reginald and Davila.⁵

3.2 Flat Fielding

Other noises associated with CCDs are sensitivity variations from photosite-to-photosite on the CCD detector or across the detector. Modern CCDs are uniform to better than 1% between neighboring photosites and uniform to better than 10% across the entire surface. Also, any sensitivity variation from pixel to pixel can be removed through flat fielding. For the polarization camera used in the ISCORE instrument, the flat fielding file has already been generated by the camera manufacturer and is built into the software package that runs the polarization camera and automatically corrects all images for flat fielding. The final processed image would then be obtained from subtracting the dark image from the raw image and dividing by the flat field image [(raw image—dark image)/flat fielding or (raw image/flat fielding—dark image/flat fielding)]. Here, through a crude experiment, we have explored the reliability of the manufacturer provided flat fielding file built into the operating software of the camera. To test this concept, we first illuminated the CCD in the polarization camera with white light that was unfocused, unpolarized, and passed through two diffusers and 10 images were captured with the built-in flat fielding corrector in the software switched off and we will call the average of these 10 images as FF_{off,T_1} , where T_1 is the integration time that allowed to record $\sim 25,000$ digital counts in majority of the pixels. Then we captured three dark images that matched the integration time T_1 with the white-light lamp and the built-in flat fielding corrector in the software switched off and we will call the average of these dark images as D_{off,T_1} . Then the gain (G) is obtained from $\frac{m}{FF_{\text{off},T_1} - D_{\text{off},T_1}}$, where m is the average of the difference $FF_{\text{off},T_1} - D_{\text{off},T_1}$. Next, an image was taken by the polarization camera with the built-in flat fielding corrector in the software switched off and we call this I_{off,T_2} , where T_2 is the integration time. Again, three dark images were taken with an integration time T_2 and the built-in flat fielding corrector in the software switched off and the average of these three we will call D_{off,T_2} . Now the same image and the dark images were taken with an integration time of T_2 , but this time with the built-in flat fielding corrector in the software switched on and we will call these I_{on,T_2} and D_{on,T_2} , respectively. Now, Figs. 4(a)–4(c), show the following: $(I_{\text{off},T_2} - D_{\text{off},T_2}) \times G$, $I_{\text{on},T_2} - D_{\text{on},T_2}$, and the difference between the two, respectively. The bottom image confirms that the majority of the differences are located close to the zero value as seen from the color coded bar that interprets the data and confirms that the laboratory generated flat fielding file does not qualitatively or quantitatively alter the final image from using the flat fielding file built-in to the operating software of the camera. However, individual pixels could degrade with time and optical systems in the ISCORE instrument can introduce sensitivity variation in the CCD, for example, vignetting. To account for these sensitivity variations, we will generate our own flat fielding file at the time and location of our experiment by taking multiple images through pointing the ISCORE instrument toward cloudless parts of the blue sky. The straight forward way to perform the comparison shown in Fig. 4 is to compare the flat fielding file created in the

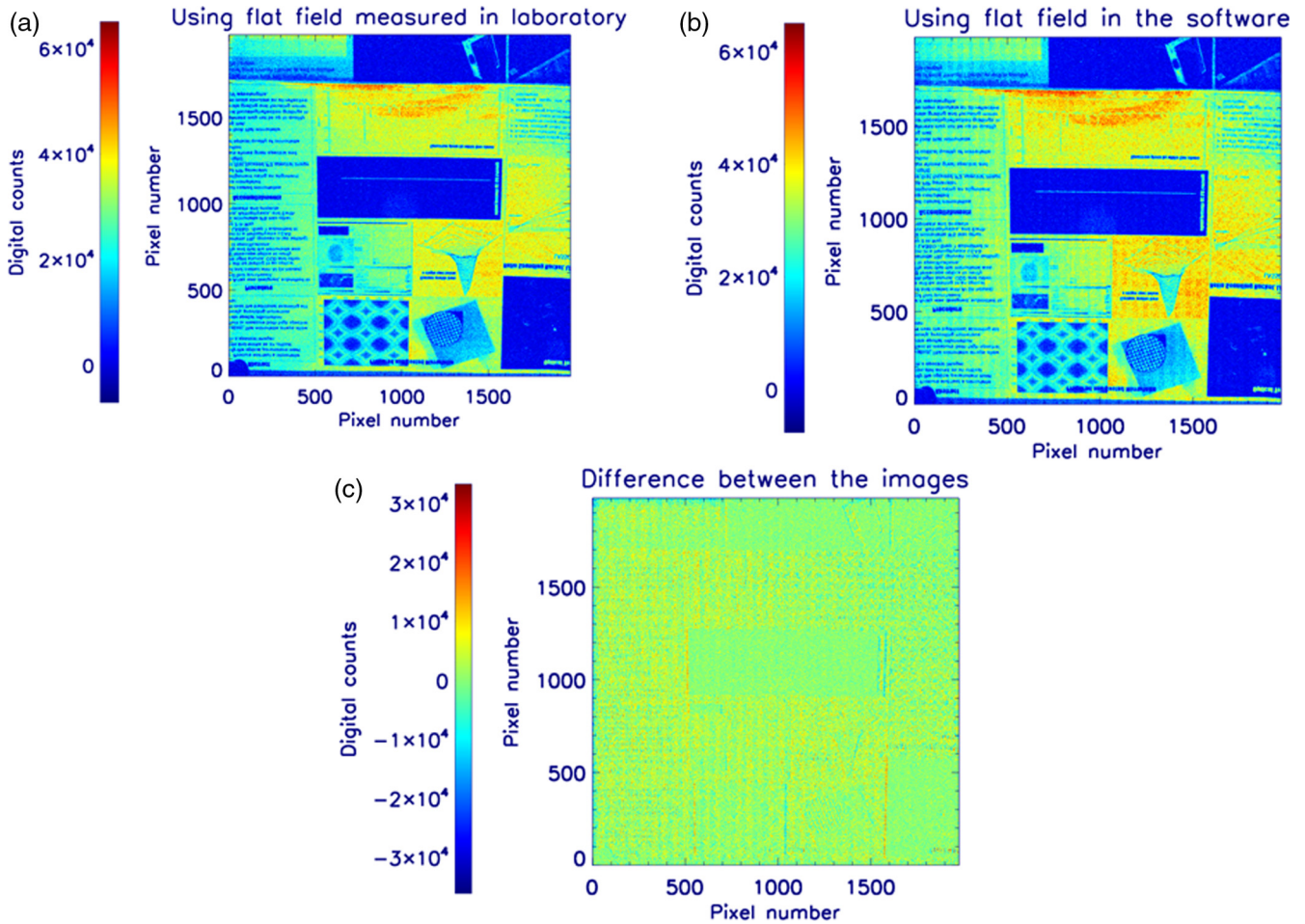


Fig. 4 (a) $(I_{\text{off},T_2} - D_{\text{off},T_2}) \times G$, (b) $I_{\text{on},T_2} - D_{\text{on},T_2}$, and (c) the difference between the two. The panel (c) shows that the majority of the differences are located close to the zero value as seen from the color coded bar that interprets the data and confirms that the laboratory generated flat field file does not qualitatively or quantitatively alter the final image from using the flat field file built into the operating software of the camera. However, pixels could degrade with time and as a precaution, we will generate our own flat fielding file at the time and location of our experiment and will use that for image processing.

laboratory with the flat fielding file embedded in the camera software and both these were created without any lenses attached to the polarization camera. Unfortunately, we do not have access to the flat fielding file embedded in the camera software.

3.3 Systematic Error

Here, we quantify the systematic error ($\sigma_{\text{systematic}}$) associated with the extinction ratio of the micropolarizer array through a laboratory experiment by passing stabilized white light through two filters centered at 385.0 and 410.0 nm with FWHM of 5.0 nm, which will determine the temperature. The ISCORE experiment measures the temperature from the polarized intensity ratios from these two filters and the magnitude of the extinction ratios at wavelengths 385.0 and 410.0 nm will determine the magnitude of the associated systematic errors in the temperature measurements. Figure 5 shows the picture of the experimental setup. The optical components of the entire experimental were mounted on a stabilized optical table and the baffling around

the optical elements (not shown in Fig. 5) ensured that light from the lamp that bounced off the walls outside of the optical elements did not reach the detector (diode or polarization camera). The entire experiment including the baffling was further enclosed inside a large light-tight black box that also included a light-tight lid (not shown in Fig. 5). The light-tightness to stray light was confirmed by first measuring the ambient light signal using the diode with all the lights in the laboratory including the lamp switched off. Then the ambient light signal was measured between the baffling and the walls of the black box with the lamp switched on and the diode reading in both cases were in the 10^{-12} Amperes ($10^{-12} \text{ A} = 1 \text{ pA}$) range and was not significant compared to the diode reading along the optical axis, which measured in the 10^{-6} Amperes ($10^{-6} \text{ A} = 1 \mu\text{A}$) range.

Then with the lamp on and light passing through the 410.0-nm filter and the Hammamatsu diode connected to a Keithley 6517B electrometer with measurement sensitivity in the pA range, diode readings were recorded by remotely turning linear polarizer 2 in intervals of 5 deg over a complete turn of 360 deg

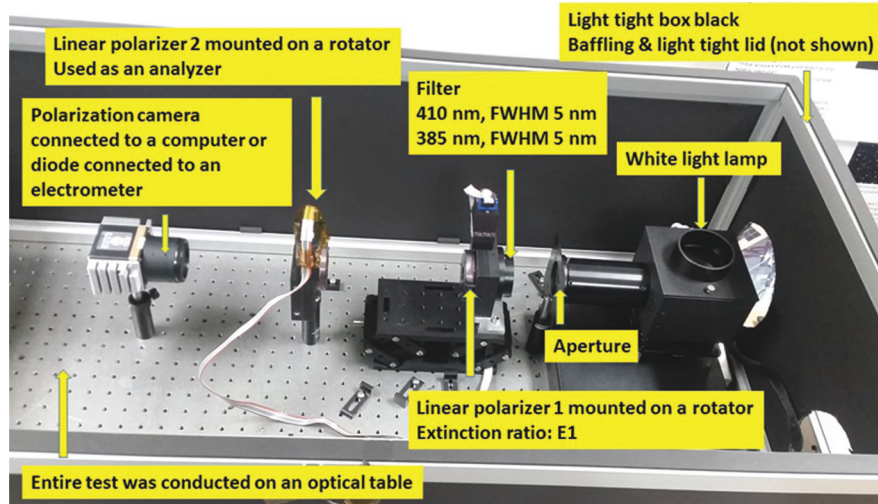


Fig. 5 Picture of the experimental setup used to determine the extinction ratio of the micropolarizer array in the polarization camera. The entire experiment was conducted on an optical table. The experimental setup consisted of a stable white-light source. The light from the source passed through a bandpass filter centered at 410 nm with FWHM of 5 nm (or 385 nm with FWHM of 5 nm) on to the first linear polarizer (linear polarizer 1). The light from linear polarizer 1 then passed through a second linear polarizer (linear polarizer 2) to a diode (or polarization camera). The two linear polarizers, linear polarizers 1 and 2, were mounted on a computer controlled rotator that could be rotated in intervals of 1 deg. When the diode was used, the current was read using a Keithley electrometer and when the polarization camera was used, the images were read using the camera software. Not shown in the picture are the baffling and the light tight lid to the black box.

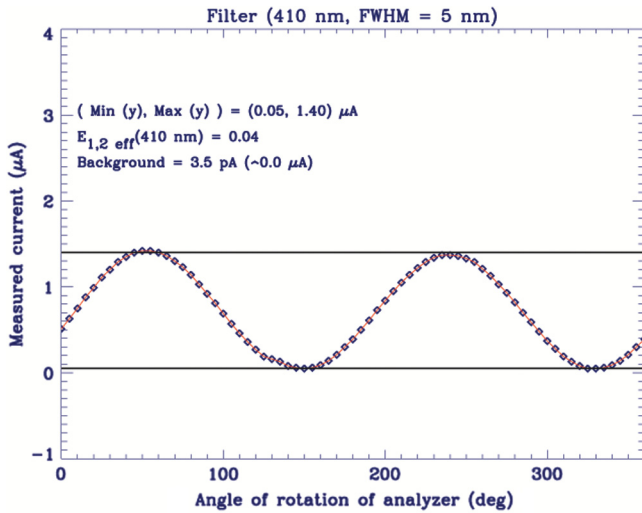


Fig. 6 Diode current reading from the experimental setup shown in Fig. 5. Here, the lamp was turned on and light passed through the 410.0-nm filter and linear polarizer 1 before passing through linear polarizer 2, which was remotely turned in intervals of 5 deg over a complete turn of 360 deg. The effective extinction ratio $E_{1,2 \text{ eff}}^{410 \text{ nm}}$ of linear polarizers 1 and 2 was measured to be 0.04. With both linear polarizers 1 and 2 determined to be almost identical, it is reasonable to claim that each of the linear polarizers 1 and 2 has individual extinction ratios $E_1^{410 \text{ nm}}$ and $E_2^{410 \text{ nm}}$, respectively, and equal to $E_{1,2 \text{ eff}}^{410 \text{ nm}}/2$ or 0.02.

and the recorded readings are plotted in Fig. 6. Figure 6 was then used to determine the effective extinction ratio ($E_{1,2 \text{ eff}}^{410 \text{ nm}}$) of the combined linear polarizer 1 and linear polarizer 2, which was measured to be 0.04. With both linear polarizer 1 and linear

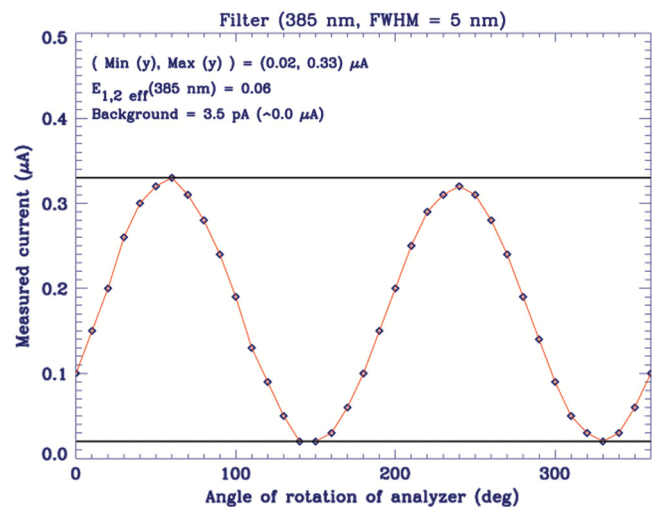


Fig. 7 Diode current reading from the experimental setup shown in Fig. 5. Here, the lamp was turned on and light passed through the 385.0-nm filter and linear polarizer 1 before passing through linear polarizer 2, which was remotely turned in intervals of 5 deg over a complete turn of 360 deg. The effective extinction ratio $E_{1,2 \text{ eff}}^{385 \text{ nm}}$ of linear polarizers 1 and 2 was measured to be 0.06. With both linear polarizers 1 and 2 determined to be almost identical, it is reasonable to claim that each of the linear polarizers 1 and 2 has individual extinction ratios $E_1^{385 \text{ nm}}$ and $E_2^{385 \text{ nm}}$, respectively, and equal to $E_{1,2 \text{ eff}}^{385 \text{ nm}}/2$ or 0.03.

polarizer 2 determined to be almost identical, it is reasonable to claim that each of the linear polarizers 1 and 2 has individual extinction ratios $E_1^{410 \text{ nm}}$ and $E_2^{410 \text{ nm}}$, respectively, and equal to $E_{1,2 \text{ eff}}^{410 \text{ nm}}/2$ or 0.02. Figure 7 is similar to Fig. 6 with the 410.0-nm

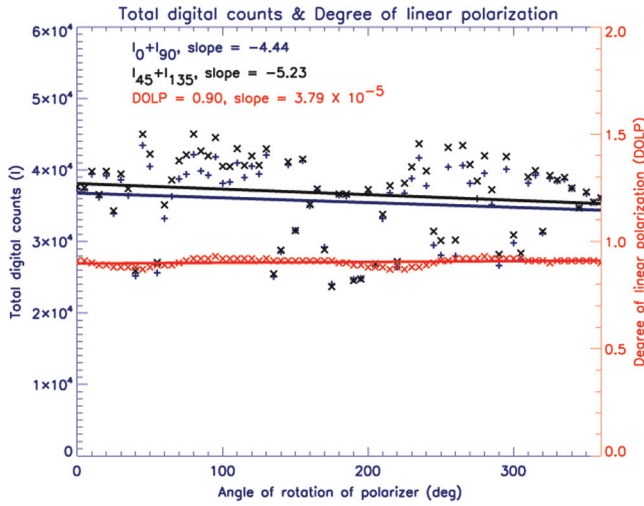


Fig. 8 Total digital counts ($I_0 + I_{90}$) and ($I_{45} + I_{135}$) measured through the 410.0-nm filter for the polarization states (P000 + P090) and (P045 + P135), respectively, and the DOLP and the three quantities show near uniformity as linear polarizer 1 was turned through 360 deg in intervals of 5 deg with slopes of -4.44 , -5.23 , and 3.79×10^{-5} , respectively. This figure also confirms the stability of the lamp.

filter replaced with the 385.0-nm filter and $E_1^{385 \text{ nm}}$ and $E_2^{385 \text{ nm}}$ equal to $E_{1,2 \text{ eff}}^{385 \text{ nm}}/2$ or 0.03.

Now linear polarizer 2 was removed and the diode was replaced with the polarization camera. This time linear polarizer 1 was remotely turned through 5-deg intervals over a complete turn through 360 deg and images from the polarization camera were captured using the camera control software. The exposure time was maintained at a constant value of 1000 μs . Figure 8 shows the total digital counts ($I_0 + I_{90}$) and ($I_{45} + I_{135}$) of the polarization states (P000+P090) and (P045+P135), respectively, which should be constant and the DOLP. According to

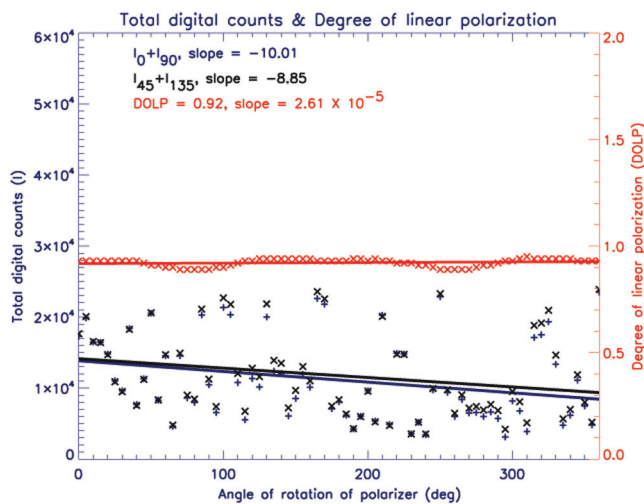


Fig. 9 Total digital counts ($I_0 + I_{90}$) and ($I_{45} + I_{135}$) measured through the 385.0-nm filter for the polarization states (P000 + P090) and (P045 + P135), respectively, and the DOLP and the three quantities show near uniformity as linear polarizer 1 was turned through 360 deg in intervals of 5 deg with slopes of -10.01 , -8.85 , and 2.61×10^{-5} , respectively. This figure also confirms the stability of the lamp.

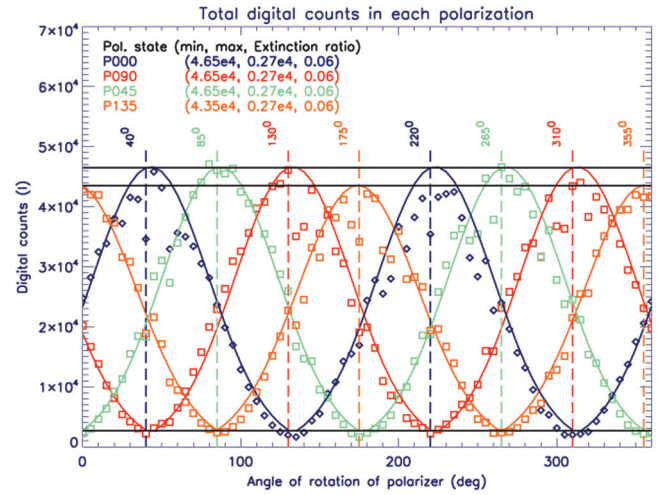


Fig. 10 Total digital counts measured by the pixels in the four polarization states in the polarization camera when linear polarizer 1 was rotated through 360 deg in intervals of 5 deg. The vertical lines are drawn through the peaks of the different polarization states and the pattern confirms that the polarization camera is operating as expected. For example, when the pixels of polarization state P090 peak we expect the pixels of polarization state P000 to bottom out and the pixels of polarization states P045 and P135 to equal and represent one half the peak value of pixels of polarization state P090. Again, when the pixels of polarization state P045 peak we expect the pixels of polarization state P135 to bottom out and the pixels of polarization states P000 and P090 to equal and represent one half the peak value of pixels of polarization state P045 and this figure amply reflects this behavior. Based on the minimum and maximum digital counts measured by each of the four polarization states the effective extinction ratios ($E_{1,PA \text{ eff}}^{410 \text{ nm}}$) due to linear polarizer 1 and PA in the polarization camera was measured to be 0.06. In creating this plot the light from the lamp passed through the 410.0 nm filter.

Fig. 8, these three quantities are uniform throughout the rotation of linear polarizer 1 through 360 deg in intervals of 5 deg with slopes of -4.44 , -5.23 and 3.79×10^{-5} , respectively, and confirms the near uniformity of the lamp throughout the experiment. Figure 9 is a repeat of Fig. 8 with the 410.0-nm filter replaced with the 385.0-nm filter and the exposure time was maintained at 2500 μs . The DOLP plots in Figs. 8 and 9 show signs of a slight oscillation and we do not have any rational answer to this observation.

Figure 10 shows the total digital counts measured by the pixels in the four polarization states, P000, P045, P090, and P135 in the polarization camera with linear polarizer 2 removed and linear polarizer 1 rotated through 360 deg in intervals of 5 deg. The vertical lines are drawn through the peaks of the four different polarization states and Fig. 10 confirms that the polarization camera is operating as expected. For example, when the pixels of polarization state P090 peak, we expect the pixels of polarization state P000 to bottom out and the pixels of polarization states P045 and P135 to equal and represent one half the peak value of pixels of polarization state P090. Again, when the pixels of polarization state P045 peak, we expect the pixels of polarization state P135 to bottom out and the pixels of polarization states at P000 and P090 to equal and represent one half the peak value of pixels of polarization state P045. Figure 10 amply reflects this behavior. The horizontal lines in Fig. 10 show the maximum and the minimum for the four polarization states and based on these maximum and minimum values, the

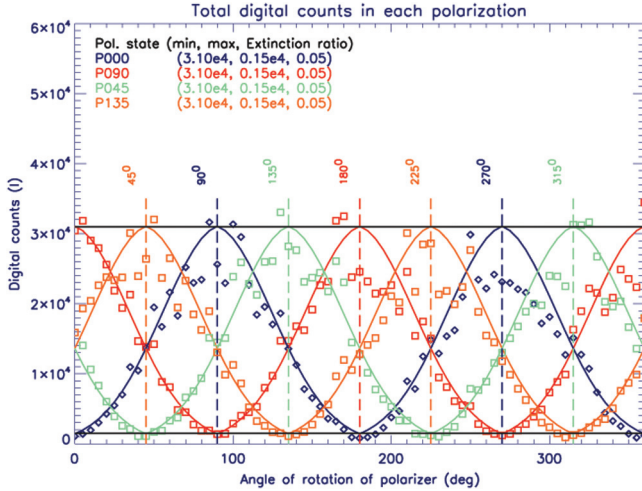


Fig. 11 Total digital counts measured by the pixels in the four polarization states in the polarization camera when linear polarizer 1 was rotated through 360 deg in intervals of 5 deg. The vertical lines are drawn through the peaks of the different polarization states and the pattern confirms that the polarization camera is operating as expected. For example, when the pixels of polarization state P090 peak we expect the pixels of polarization state P000 to bottom out and the pixels of polarization states P045 and P135 to equal and represent one half the peak value of pixels of polarization state P090. Again when the pixels of polarization state P045 peak we expect the pixels of polarization state P135 to bottom out and the pixels of polarization states P000 and P090 to equal and represent one half the peak value of pixels of polarization state P045 and this figure amply reflects this behavior. Based on the minimum and maximum digital counts measured by each of the four polarization states, the effective extinction ratios ($E_{1,PA\text{eff}}^{385\text{ nm}}$) due to linear polarizer 1 and PA in the polarization camera were measured to be 0.05. In creating this plot, the light from the lamp passed through the 385.0-nm filter.

effective extinction ratios ($E_{1,PA\text{eff}}^{410\text{ nm}}$) due to linear polarizer 1 and PA in the polarization camera were measured to be 0.06. Figure 11 is analogous to Fig. 10 with the 410.0-nm filter replaced with the 385.0-nm filter.

Now with the measured extinction ratios $E_{1,PA\text{eff}}^\lambda$ and E_1^λ , we will be able to determine the extinction ratio E_{PA}^λ from the following mathematical formulation, shown as a schematic diagram in Fig. 12. Then with the derived values for E_{PA}^λ at the two wavelength position 410.0 and 385.0 nm, we will be able to determine the associated systematic error in determining the electron temperature using the ISCORE instrument.

In Fig. 12, if S is the light of intensity passing through the axis of polarization (Y -axis) of linear polarizer 1, then the light passing along the X -axis of linear polarizer 1 will be SE_1^λ , where E_1^λ is the extinction ratio of linear polarizer 1. Then if E_{PA}^λ is the extinction ratio of the PA and if the polarization state $P^\lambda(\theta)$ is parallel to the Y -axis of linear polarizer 1, then the polarization state $P^\lambda(\theta + 90\text{ deg})$ will be parallel to the X -axis in linear polarizer 1 and the intensity I_0^λ and $I_{0+90\text{ deg}}^\lambda$ along $P^\lambda(\theta)$ and $P^\lambda(\theta + 90\text{ deg})$, respectively, that will be directed toward the CCD detector is given by Eq. (5). Table 3 lists the values of E_{PA}^λ measured for the two wavelengths 385.0 and 410.0 nm from the laboratory tests conducted by the authors of this paper and at 550.0 nm from the manual made available by the manufacturer of the polarization camera, which are 0.02, 0.04, and 0.02, respectively. In Fig. 12, we have assumed that the incident light on the PA is transmitted on to the CCD detector without any transmission loss. Even if the transmission efficiency was less than 100%, this contribution would cancel off in Eq. (5) because both the numerator and denominator will be multiplied by the transmission efficiency coefficient of the PA:

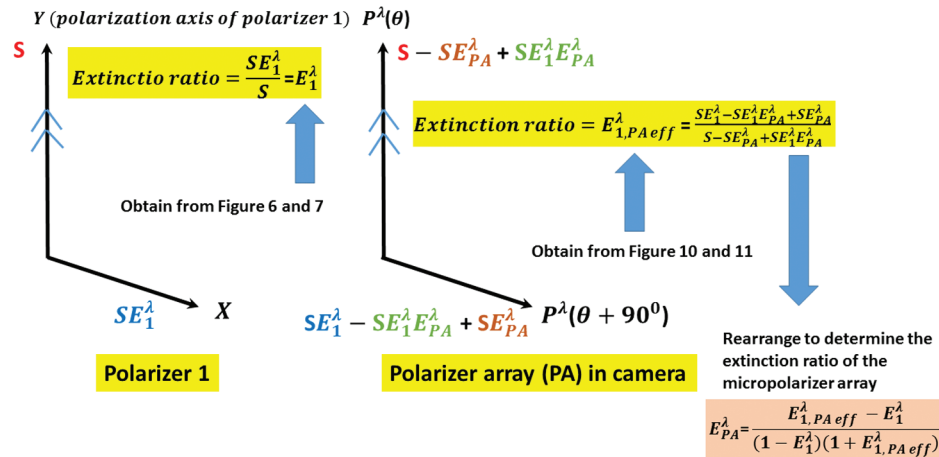


Fig. 12 Schematic diagram showing the formulation to determine the extinction ratio E_{PA}^λ of the PA. The extinction ratios E_1^λ for the two wavelengths 410.0 and 385.0 nm were determined from Figs. 6 and 7, respectively, and the effective extinction ratios $E_{1,PA\text{eff}}^\lambda$ of linear polarizer 1 and PA for the same two wavelengths were determined from Figs. 10 and 11, respectively. This schematic diagram assumes light of intensity S passes along the axis of polarization (Y -axis) of linear polarizer 1 and based on its extinction ratio E_1^λ light of intensity SE_1^λ will pass through the orthogonal X -axis in linear polarizer 1. If a polarization state $P^\lambda(\theta)$ of the PA is parallel to the Y -axis of linear polarizer 1 then polarization state $P^\lambda(\theta + 90\text{ deg})$ will be parallel to the X -axis of linear polarizer 1. In this configuration, the schematic diagram shows the fractions of light intensity that gets distributed along $P^\lambda(\theta)$ and $P^\lambda(\theta + 90\text{ deg})$ as a function of E_1^λ and E_{PA}^λ , where E_{PA}^λ is unknown and needs to be determined.

Table 3 E_{PA}^λ derived from Eq. (5) for the two wavelengths 410.0 and 385.0 nm using E_1^λ from Figs. 6 and 7 and $E_{1,\text{PAeff}}^\lambda$ from Figs. 10 and 11. The polarization camera manual specifies an extinction ratio of 0.02 at 550.0 nm for the PA.

λ (nm)	E_1^λ	$E_{1,\text{PAeff}}^\lambda$	E_{PA}^λ
410	0.02	0.06	0.04
385	0.03	0.05	0.02
550	NA	NA	0.02

Note: NA, not applicable.

$$\begin{aligned}
 I_0^\lambda &= S - SE_{\text{PA}}^\lambda + SE_1^\lambda E_{\text{PA}}^\lambda, \\
 I_{(\theta+90 \text{ deg})}^\lambda &= SE_1^\lambda + SE_{\text{PA}}^\lambda - SE_1^\lambda E_{\text{PA}}^\lambda, \\
 E_{1,\text{PAeff}}^\lambda &= \frac{I_{(\theta+90 \text{ deg})}^\lambda}{I_0^\lambda}, \\
 E_{\text{PA}}^\lambda &= \frac{E_{1,\text{PAeff}}^\lambda - E_1^\lambda}{(1 - E_1^\lambda)(1 + E_{1,\text{PAeff}}^\lambda)}. \quad (5)
 \end{aligned}$$

In creating Table 3, we have considered light passing from one axis to another through the extinction ratio process, as

$$\begin{aligned}
 (I_\theta^\lambda)^{\text{measured}} &= I_\theta^\lambda + I_{(\theta+90 \text{ deg})}^\lambda E_{\text{PA}}^\lambda - I_\theta^\lambda E_{\text{PA}}^\lambda, \\
 (I_{(\theta+90 \text{ deg})}^\lambda)^{\text{measured}} &= I_{(\theta+90 \text{ deg})}^\lambda + I_\theta^\lambda E_{\text{PA}}^\lambda - I_{(\theta+90 \text{ deg})}^\lambda E_{\text{PA}}^\lambda, \\
 \text{where } \theta &= 0 \quad \text{and} \quad 45 \text{ deg}.
 \end{aligned}$$

$$\begin{aligned}
 \text{pB}^{\text{MR}} &= \frac{\sqrt{[(I_0^{410})^{\text{measured}} - (I_{90}^{410})^{\text{measured}}]^2 + [(I_{45}^{410})^{\text{measured}} - (I_{135}^{410})^{\text{measured}}]^2}}{\sqrt{[(I_0^{385})^{\text{measured}} - (I_{90}^{385})^{\text{measured}}]^2 + [(I_{45}^{385})^{\text{measured}} - (I_{135}^{385})^{\text{measured}}]^2}}, \\
 \text{pB}^{\text{MR}} &= \text{pB}^{\text{TR}} \frac{(1 - 2E_{\text{PA}}^{410})}{(1 - 2E_{\text{PA}}^{385})}, \\
 \text{pB}^{\text{MR}} &= \frac{I_p^{410}}{I_p^{410}} \frac{(1 - 2E_{\text{PA}}^{410})}{(1 - 2E_{\text{PA}}^{385})}, \\
 \rightarrow \text{pB}^{\text{MR}} &= f(I_p^\lambda, E_{\text{PA}}^\lambda). \quad (7)
 \end{aligned}$$

Now from Eq. (7), we can estimate $\sigma_{\text{systematic}}$ in the measured pB, which is given by Eq. (8) by using the values for E_{PA}^λ from Table 3. It was shown by Reginald et al.⁵ that an uncertainty of $\pm 1\%$ in “measured” pB^{MR} can generate an uncertainty in the “measured” electron temperature by ± 0.2 MK. Therefore, with a derived systematic error of -4% from Eq. (8), the measured electron temperature will be underestimated by 0.8 MK:

$$\begin{aligned}
 \sigma_{\text{systematic}} &= \frac{\text{pB}^{\text{MR}} - \text{pB}^{\text{TR}}}{\text{pB}^{\text{TR}}} = \frac{(1 - 2E_{\text{PA}}^{410})}{(1 - 2E_{\text{PA}}^{385})} - 1, \\
 \sigma_{\text{systematic}} &= \frac{2(E_{\text{PA}}^{385} - E_{\text{PA}}^{410})}{(1 - 2E_{\text{PA}}^{385})} = -0.04(\text{or } -4\%), \\
 \rightarrow \text{temperature under estimation} &\approx 0.8 \text{ MK}. \quad (8)
 \end{aligned}$$

schematically shown in Fig. 12, although this process is not unique. A more rigorous form of conducting this measurement would be through matrix formulation of the measurement process based on the estimates of the Muller matrix of the polarizer coupled with the measurement matrix that will convert the Stokes vectors to the four channels in the CCD super pixel. However, we do not have the Muller matrix estimates of the polarizers used in this test from the original vendors and will consider implementing this process at a later time.

Now using the extinction ratios E_{PA}^λ from Table 3, we can estimate the systematic error in temperature measurements. To measure the temperature, we need to determine the “true” linearly polarized brightness ratio (pB^{TR}), as defined by Eq. (4), and is given by Eq. (6):

$$\text{pB}^{\text{TR}} = \frac{\sqrt{(I_0^{410} - I_{90}^{410})^2 + (I_{45}^{410} - I_{135}^{410})^2}}{\sqrt{(I_0^{385} - I_{90}^{385})^2 + (I_{45}^{385} - I_{135}^{385})^2}}. \quad (6)$$

However, with nonzero E_{PA}^λ values for the two wavelengths, the “measured” linearly polarized brightness ratio (pB^{MR}) is given by Eq. (7), where we have used the same logical arguments shown in Fig. 12 to derive the “measured” $(I_\theta^\lambda)^{\text{measured}}$ and $(I_{(\theta+90 \text{ deg})}^\lambda)^{\text{measured}}$ for the two polarization state pairs (P000, P090) and (P045, P135):

Equation (9) shows the “measured” total brightness tB^{MR} using the analogy from Fig. 12 and it is apparent that tB^{MR} is a function of both the polarized I_p^λ and unpolarized I_u^λ light, but is not a function of the extinction ratios E_{PA}^λ . Figure 6 by Reginald et al.⁴ shows the “theoretically” modeled “temperature sensitive intensity ratio” (TSIR) plotted against electron temperature (T) in the corona based on photospheric light passing through the two color filters centered at 410.0 and 385.0 nm. TSIR, as defined in Eq. (9), is a special case of tB^{MR} with I_u equal to zero and this condition can be satisfied only in the low solar corona close to the solar limb, as evident in Fig. 1, where the linearly polarized K-corona brightness is much greater than the unpolarized F-corona brightness. Therefore, in the past ISCORE experiments, we limited our observations to low coronal regions close to the solar limb and assumed our measurements to satisfy the conditions to obtain TSIR and we

interpreted the “measured” TSIR for electron temperature using Fig. 6 by Reginald et al.⁴ Here, we wish to note that tB^{MR} cannot be used to determine the electron temperature since it also contains I_u^λ and will need a separate I_u^λ model or experimental results

$$\begin{aligned}
 (I_\theta^\lambda)^{\text{measured}} &= I_\theta^\lambda + I_{(\theta+90 \text{ deg})}^\lambda E_{PA}^\lambda - I_\theta^\lambda E_{PA}^\lambda, \\
 (I_{(\theta+90 \text{ deg})}^\lambda)^{\text{measured}} &= I_{(\theta+90 \text{ deg})}^\lambda + I_\theta^\lambda E_{PA}^\lambda - I_{(\theta+90 \text{ deg})}^\lambda E_{PA}^\lambda, \\
 tB^{MR} &= \frac{[(I_0^{410})^{\text{measured}} + (I_{45}^{410})^{\text{measured}} + (I_{90}^{410})^{\text{measured}} + (I_{135}^{410})^{\text{measured}}]/2}{[(I_0^{385})^{\text{measured}} + (I_{45}^{385})^{\text{measured}} + (I_{90}^{385})^{\text{measured}} + (I_{135}^{385})^{\text{measured}}]/2}, \\
 tB^{MR} &= \frac{I_u^{410} + I_p^{410}}{I_u^{385} + I_p^{385}}, \\
 \rightarrow tB^{MR} &= f(I_p^\lambda, I_u^\lambda), \\
 tB^{MR}(I_u^\lambda = 0) &= \frac{I_p^{410}}{I_p^{385}} = \text{TSIR}.
 \end{aligned} \tag{9}$$

Figure 13 shows the theoretically modeled polarized brightness ratio $pB^{\text{Theo.R}}$ plotted against assumed thermal electron temperatures (T) in the corona based on photospheric light passing through the two color filters centered at 410.0 and 385.0 nm. Now, Fig. 13 is similar to Fig. 6 by Reginald et al.⁴ and can be used to interpret the measured pB^{MR} given by Eq. (7) for electron temperature.

Table 4 lists in column 1 the possible measurable quantities — pB^{MR} , tB^{MR} , and TSIR—that can be used to determine the electron temperature and their dependence on I_p^λ , I_u^λ , and E_{PA}^λ based on the type of camera used and whether a linear polarizer is used or not. By default, the polarization camera does have a built-in linear polarizer embedded on the CCD. The linear polarizer used with the regular (nonpolarization) camera is assumed to be an external linear polarizer with very high extinction ratio mounted on a rotator mechanism and images taken by rotating the linear polarizer through three well-defined angles.

From Table 4, measuring TSIR, although it is not a function of E_{PA}^λ , in both polarization and regular cameras, it assumes to

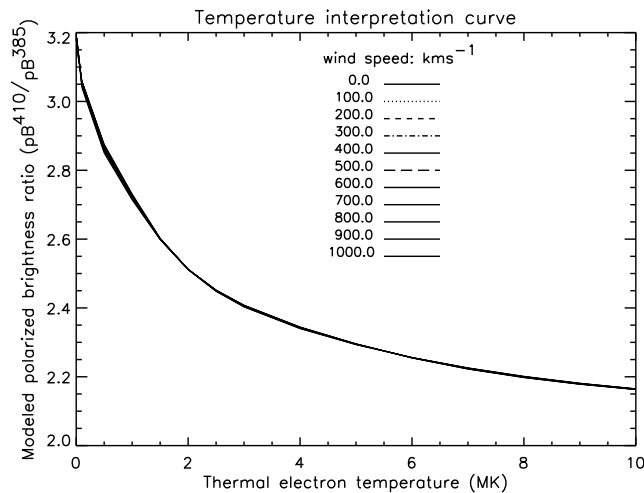


Fig. 13 Theoretically modeled polarized brightness ratio $pB^{\text{Theo.R}}$ plotted against assumed thermal electron temperatures in the corona based on sun light passing through the same two color filters centered at 410.0 and 385.0 nm used in the laboratory tests. The ISCORE experiment will determine electron temperature by interpreting measured linearly polarized brightness ratio pB^{MR} using this plot.

to correct tB^{MR} . On the other hand, TSIR, if limited to low solar coronal regions, is not subject to any systematic errors associated with E_{PA}^λ of the micropolarizer array in the polarization camera:

be free of unpolarized light. As a result, TSIR can be used to determine the electron temperature only in the very low coronal region up to $1.5 R_\odot$ from the sun center, where the linearly polarized K-coronal brightness is much greater than the unpolarized F-coronal brightness, as evident in Fig. 1. On the other hand, pB^{TR} measured using a polarization camera, although it is a function of E_{PA}^λ and will generate a systematic error that requires accurate quantification, will be free of unpolarized light. While pB^{TR} measured using a regular camera will not be a function of E_{PA}^λ but will require the use a polarization wheel mounted on a rotator mechanism to measure pB^{TR} , which runs contrary to our main objective of eliminating the need to turn a linear polarizer through three angles in order to preserve temporal resolution. As noted earlier, the quantity tB^{TR} cannot be used for temperature interpretation because of the presence of unpolarized light. Another very important reason to use pB^{TR} for temperature interpretation stems from the need to measure electron temperatures at coronal heights above $1.5 R_\odot$ from the sun center. To elaborate, as evident in Fig. 1, the linearly polarized K-coronal brightness will match the unpolarized F-coronal brightness around $2 R_\odot$ from the sun center and beyond that the F component will always be greater than the K component. Thus, in order to extend beyond the low coronal region for temperature measurements, we will either have to use a regular camera with a polarization wheel

Table 4 The possible measurable quantities using a polarization camera or a regular (nonpolarization) camera and their dependence on I_p^λ , I_u^λ , and E_{PA}^λ based on the type of camera used and whether a linear polarizer is used or not. By default, the polarization camera does use the micropolarizer array embedded on the camera. The linear polarizer used with the regular camera is assumed to be an external linear polarizer with very high extinction ratio mounted on a rotator mechanism and images taken by rotating the linear polarizer by three well-defined angles.

Measured quantity	Polarization camera/ linear polarizer	Regular camera/ linear polarizer
pB^{MR}	$f(I_p^\lambda, E_{PA}^\lambda)$, yes	$f(I_p^\lambda)$, yes
tB^{MR}	$f(I_p^\lambda, I_u^\lambda)$, yes	$f(I_p^\lambda, I_u^\lambda)$, no
TSIR	$f(I_p^\lambda)$, yes	$f(I_p^\lambda)$, no

mounted on a rotator mechanism and lose temporal resolution or use a polarization camera and improve the temporal resolution but introduce a systematic error. However, if we can accurately measure this systematic error, then we will be able to use the polarization camera to measure the electron temperature from $(1 - 4) R_{\odot}$ from the sun center.

$\sigma_{\text{systematic}}$ of 0.8 MK derived from Eq. (8) was from laboratory experiments. But this same systematic error could also be quantified through coronal observations made through the two

color filters using the polarization camera during a total solar eclipse. To do so, first, from Table 4, we can measure electron temperature using TSIR at locations very close to solar limb and we will call it T^{TSIR} . Second, at the same position as the first, we can also measure pB^{MR} and derive the electron temperature and we will call it T^{PB} , which will be offset by the systematic error. Therefore, the difference in temperature from $(T^{\text{TSIR}} - T^{\text{PB}})$ should match the systematic error shown in Eq. (8) and this verification process is summarized in Eq. (10):

Very close to the solar limb (pB or K-corona) \gg (uB or F-corona) \Rightarrow TSIR = $f(I_p^{\lambda})$ is valid

\Rightarrow TSIR measures electron temperature T^{TSIR} .

But $\text{pB}^{\text{MR}} = f(I_p^{\lambda}, E_{\text{PA}}^{\lambda})$

\Rightarrow pB^{MR} measures electron temperature T^{PB}

$\Rightarrow (T^{\text{TSIR}} - T^{\text{PB}}) \simeq$ systematic error (or 0.8 MK). (10)

In this paper, we have not shown the measurement of the extinction ratios of the two filters centered at 398.7 and 423.3 nm with FWHM of 5.0 nm that will be used to determine the speed. To determine the speed at a given super pixel, first, we have to determine the temperature for that super pixel. Then using the measured temperature for that super pixel as the model temperature for that super pixel, we have to create theoretically modeled polarized brightness ratio $\text{pB}^{\text{Theo.R}}$ for assumed solar wind speeds in the corona based on sun light passing through the two speed sensitive color filters centered at 423.3 and 398.7 nm. This plot will have modeled values of $\text{pB}^{423.3} / \text{pB}^{398.7}$ along the ordinate and assumed wind speeds in the abscissa (for example, see Fig. 3 by Reginald and Davila⁵). Finally, the “measured” linearly polarized brightness ratio measured from the images taken through the 398.7 and 423.3 nm filters will be compared with the modeled ratio for the same two wavelengths to interpret wind speeds. This process for temperature and wind speed determination will be applied for each super pixel that is exposed to the solar corona.

3.4 Total Error

We have shown how the σ_{random} and $\sigma_{\text{systematic}}$ could be determined for each super pixel and will quantify the error margins associated with the electron temperature and speed measured for each super pixel.

3.5 Other Camera Characteristics

From the characterization experiments conducted on the camera, we can now show by example to prove how well the polarization camera was able to reproduce a known physical parameter, as illustrated in Fig. 14. Figure 14 shows the four states of polarization—P000, P045, P090, and P135—which are separated from their immediate neighbors to the right and left by 45 deg with the polarization axis of linear polarizer 1 oriented at θ from the reference point, which is the direction of the P000 state. For each image taken by the polarization camera, the AOLP could be determined from Eq. (2). Now, if linear polarizer 1 was turned counterclockwise in 5-deg interval over a complete circle, then the successive measurements of AOLP also should change by 5 deg.

Figures 15 and 16 show the derived AOLP using Eq. (2) for the two filters 410.0 and 380.0 nm, respectively, with linear

polarizer 1 turned through 360 deg in intervals of 5 deg. The horizontal and vertical lines in Figs. 15 and 16 need to be compared with the similarly colored vertical lines in Figs. 10 and 11, respectively, which are drawn through the maximum points in the counts registered by the different polarization states. For example, in Fig. 16, linear polarizer 1 starts with its polarization axis oriented along the P090 polarization state, which is proven in Fig. 11 with polarization state P090 showing the maximum counts at the start of linear polarizer 1. In this case, the measured AOLP at the starting point of linear polarizer 1 could be labeled as 90 or 270 deg, as evident in Fig. 16, and we chose AOLP to be 270 deg at the starting point of linear polarizer 1. Then when linear polarizer 1 was rotated counterclockwise by 90 deg, the AOLP was zero, and in Fig. 11, the polarization axis of linear polarizer 1 coincided with the maximum point of P000

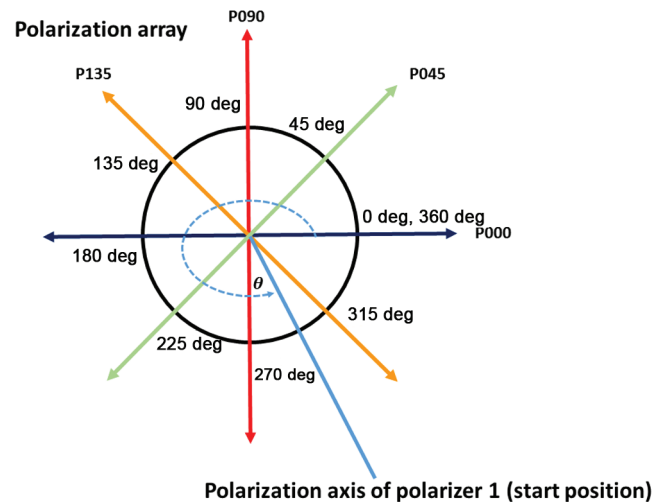


Fig. 14 Schematic diagram showing the four states of polarization, P000, P045, P090, and P135, which are separated from their immediate neighbors to the right and left by 45 deg with the polarization axis of linear polarizer 1 oriented at θ from the reference point, which is the direction of the P000 state. For each image taken by the polarization camera, the AOLP could be determined from Eq. (2). Now, if linear polarizer 1 was turned counter clockwise in 5-deg interval over a complete circle, then the successive measurements of AOLP also should change by 5 deg.

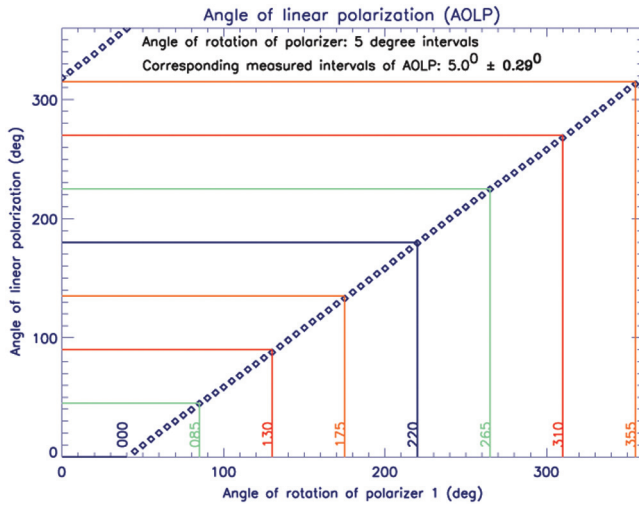


Fig. 15 Derived AOLP using Eq. (2) for the 410.0-nm filter with linear polarizer 1 turned through 360 deg in intervals of 5-deg interval. The starting position θ of linear polarizer 1 was at 320 deg, as illustrated in Fig. 14. The derived AOLP values have a difference from the immediate neighbors to the left and right by 5 ± 0.29 deg. The accuracy of the rotation of linear polarizer 1 in 5-deg interval using a computer controlled software was only verified visually.

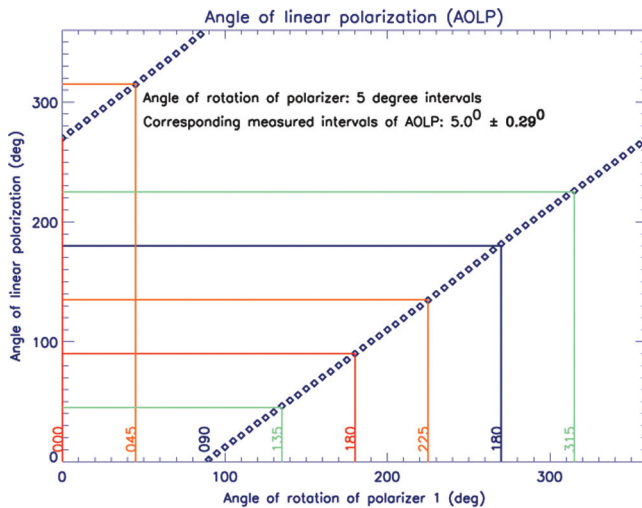


Fig. 16 Derived AOLP using Eq. (2) for the 385.0-nm filter with linear polarizer 1 turned through 360 deg in intervals of 5-deg interval. The starting position θ of linear polarizer 1 was at 270 deg, as illustrated in Fig. 14. The derived AOLP values have a difference from the immediate neighbors to the left and right by 5 ± 0.29 deg. The accuracy of the rotation of linear polarizer 1 in 5-deg interval using a computer controlled software was only verified visually.

polarization state. The other vertical lines in Fig. 16 follow the same pattern, and the colors of these vertical lines have to be compared with the vertical lines of the same colors in Fig. 11 to verify the accuracy. In Fig. 15, linear polarizer 1 starts with θ in Fig. 14 at 320 deg and when the linear polarizer 1 turned through 40 deg, the polarization axis of linear polarizer 1 coincided with the P000 polarization state, as seen in Fig. 10. In conclusion, the AOLP values derived in Figs. 15 and 16 have a difference from their immediate neighbors to the left and right by 5 ± 0.29 deg, which matches the rotation of linear polarizer 1 in 5-deg interval using a computer controlled rotator, although

its accuracy was only verified visually. The uncertainty level of 0.29 deg matches with the uncertainty level of 0.27 deg reported by Brock et al.¹⁰ in a similar experiment.

3.6 Instrumental Polarization

Finally, we also have to account for the instrumental polarization introduced by the Schmidt–Cassegrain telescope used in the ISCORE instrument where even when a truly zero polarized external source is observed through the telescope and some non-zero polarization is detected at some orientation. Even with the optical components of a Schmidt–Cassegrain telescope being axisymmetric, such telescopes can introduce their own unique instrumental polarization due to the optical coatings on the primary and the secondary mirrors. Since the orientation of the instrumental polarization is fixed, its plane of polarization will also rotate with the telescope when the telescope is rotated. A commonly used method of testing for instrumental polarization is to observe a star which is known to be unpolarized and observe if any measurable polarization is detected. Such stars are usually referred to as unpolarized standard stars and a listing of such stars is presented by Serkowski.¹¹ Since the Schmidt–Cassegrain telescope used in the ISCORE experiment is an off-the-shelf telescope and the instrumental polarization and its orientation is unique to that telescope, we will measure the instrumental polarization by observing an unpolarized star through the four filters the night before the total solar eclipse of August 21, 2017. This way, the polarized camera mounted on the telescope will stay fixed in position and in orientation to the optical axis of the telescope through the measurements for instrumental polarization, flat fielding, and observation of the corona during the eclipse.

4 Field Tests Using the Polarization Camera

We conducted several field tests in conjunction with a regular full moon to test the suitability of using the polarization camera during a total solar eclipse. Taking images of the full moon is an essential process that we have followed prior to all our past eclipse expeditions because the brightness of the full moon closely matches the brightness of a total solar eclipse (see Ref. 12) and allowed us to predetermine suitable exposure times to be used for various filters so that we do not over- or underexpose and optimally make use of the limited durations of total solar eclipses. For this purpose, we used an instrument configuration, as shown in Fig. 17, that was composed of a Meade 8-in., $F/6.3$ Schmidt–Cassegrain telescope, coupled to an $F/6.3$ focal reducer to increase the field-of-view, a filter wheel with five slots for filters with four slots mounted with the four filters centered at 385.0, 398.7, 410.0, and 423.3 nm and bandwidth of ~ 5 nm and the remaining slot left open, and finally the image was focused on to the polarization camera. This exact instrument shown in Fig. 17 was tested during the total solar eclipse of March 9, 2016, in Maba, Indonesia, but inclement weather failed us. In this configuration, the angular resolution of the sun on the polarization camera is 3.3 arcsec along with a field-of-view of $\sim 3.9 R_{\odot} \times 3.9 R_{\odot}$. We also mounted on the body of the telescope a Canon digital camera with an 800-mm zoom lens that was programmed to take continuous images in white light. These high resolution images from the Canon camera are intended to correlate with the low resolution coronal images taken by the polarization camera to identify the locations of various coronal structures like prominences and bright streamers that might be seen during the

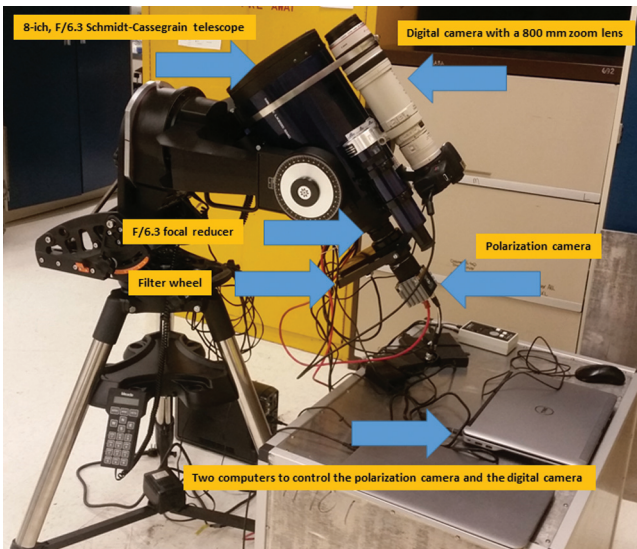


Fig. 17 Image of the ISCORE instrument that is comprised of the following as labeled: 8-in., $F/6.3$ Schmidt–Cassegrain telescope, $F/6.3$ focal reducer, filter wheel with five slots with four slots mounted with four filters that are centered at 385.0, 398.7, 410.0, and 423.3 nm with bandwidths of ~ 5 nm and one slot left open, and the polarization camera. Mounted on the telescope is a Canon digital camera with an 800-mm zoom lens that is coaligned with the polarization camera and the view finder of the telescope. This exact instrument was tested during the total solar eclipse of March 9, 2016, in Maba, Indonesia, but inclement weather failed us.

eclipse. In order to accomplish this task, we coaligned the Canon digital camera, the view finder in the telescope, and the polarization camera by focusing and centering a ground object at the center of the field in each of these three components. This coalignment also allows us to keep the moon in the center of our field by correcting for any tracking inadequacies with the use of the handheld controller that controls the right ascension and declination of the telescope.

Figure 18 shows an example of an image of a full moon taken through the 385.0-nm filter, which is the least sensitive filter of all the four filters because its wavelength center is located almost at the intersection of visible and ultraviolet spectral regions of sun light. The four images of the moon seen in Fig. 18 correspond to the image seen by the four polarization states of the pixels in the polarization camera, as explained in Fig. 2. This image required an integration time of 10 s at 16-bit digitization, whereas similar images through the other three filters centered at 398.7, 410.0, and 423.3 nm required only 3, 2, and 2 s exposures, respectively. At this rate, we expected to obtain 8, 18, 16, and 17 images of the corona through the four filters centered at 385.0, 398.7, 410.0, and 423.3 nm, respectively, during the total solar eclipse of March 9, 2016, that lasted for 199 s. Figures 19–21 show the total brightness, linearly polarized brightness, and unpolarized brightness, respectively, as derived from Fig. 18 using Eq. (4). In the context of a total solar eclipse, we expect Figs. 19–21 to represent total brightness ($K+F$), linearly polarized brightness (K), and unpolarized brightness (F) of the solar corona, respectively.

From Fig. 20, we see that the sun light reflected off the moon’s surface has a polarized component although the sun light itself is known to be unpolarized. This finding is supported by Heiles,¹³ who has shown that the moon light, to an extent, is linearly polarized and is strongly dependent on the lunar phase angle. According to Heiles,¹³ if the moon were an optically

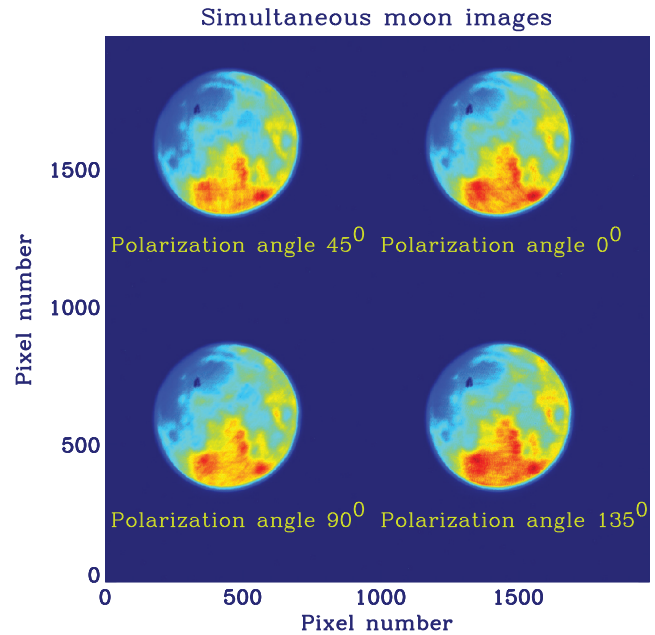


Fig. 18 Image of the full moon taken by the ISCORE instrument through the filter centered at 385.0 nm. Each image taken through the polarization camera produces four images that show the intensities through four polarization angles 0, 45, 90, and 135 deg. The integration time for this image was 10 s at 16-bit digitization. The tiny blue speck seen on the moon’s surface around 10 o’clock is a dust speck on the CCD in the polarization camera, which was eventually removed using a puffer.

smooth dielectric sphere, then we would measure 100% linear polarization perpendicular to the plane of incidence when the angle between the direction of the incident ray and the surface normal is equal to the Brewster angle.

Figure 22 shows the degree of linear polarization, as defined by Eq. (2), and has been used by planetary geologists to study the composition and texture of the material on lunar surface, as explained by Shkuratov et al.^{14–16} Fernside et al.¹⁷ describe the dependence of the degree of linear polarization of the moon light on the terrestrial granular material on the moon’s surface and show by examples how the granular sizes vary in different

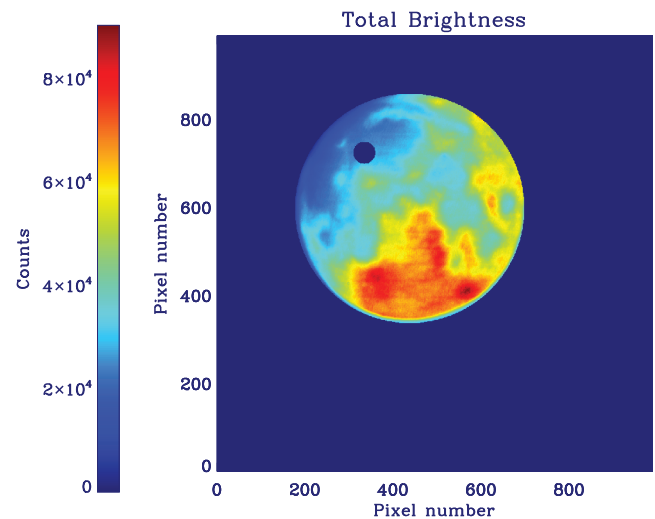


Fig. 19 The total brightness (tB) derived from Fig. 18 using Eq. (4). The dark spot on the moon is the area where the speck of dust is seen in Fig. 18.

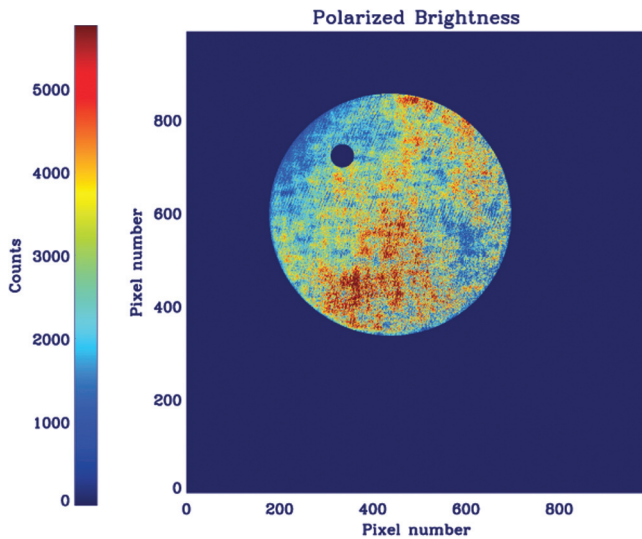


Fig. 20 The linearly pB derived from Fig. 18 using Eq. (4). The dark spot on the moon is the area where the speck of dust is seen in Fig. 18.

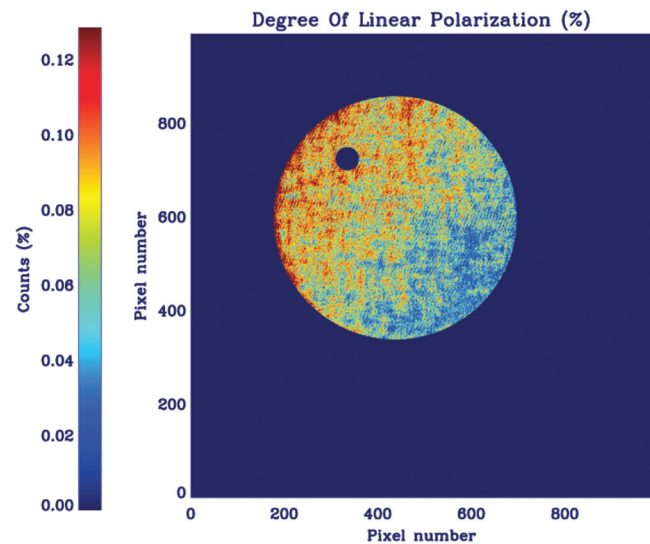


Fig. 22 DOLP derived from Fig. 18 using Eq. (2). The dark spot on the moon is the area where the speck of dust is seen in Fig. 18.

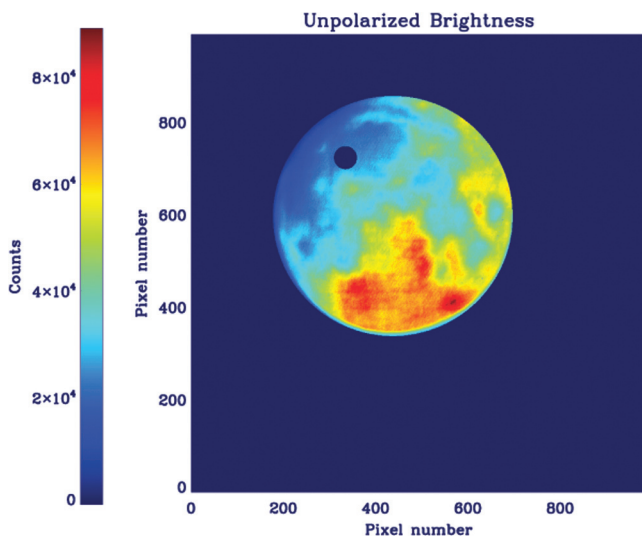


Fig. 21 The uB derived from Fig. 18 using Eq. (4). The dark spot on the moon is the area, where the speck of dust is seen in Fig. 18.

parts of the moon's surface, such as the Aristarchus Plateau and the Marius Hills, which results in different degrees of linear polarization of the sun light reflected off these locations on the moon's surface. In the above examples, large observatory facilities were used to conduct the experiments and are definitely not constrained by time. In this regard, it is remarkable that our small 8-in. off-the-shelf commercial telescope coupled to a polarization camera was able to extract the polarized component that was only $\sim 0.03\%$ to 0.12% of the total signal, as seen in Fig. 22, and has positive implications for the ISCORE instrument. This is because, as per Fig. 1, the ISCORE instrument with a practical field-of-view extending up to $4 R_{\odot}$ will be capable of measuring the K-coronal brightness, which is $\sim 10\times$ at $1 R_{\odot}$, $\sim 1\times$ at $2 R_{\odot}$ and $\sim 0.1\times$ at $4 R_{\odot}$ of the total brightness that comprises both the totally linearly polarized K-coronal brightness and the totally unpolarized F-coronal brightness.

In an experiment directly related to the low solar corona, Kim et al.¹⁸ used polarizers in three orientations to measure the S_0 ,

S_1 , and S_2 components of the Stokes vector in the visible light region. Assuming a linearly polarized K-corona, Kim et al.¹⁸ measured the 2-D distribution of the polarization angle in the low solar corona extending up to $1.4 R_{\odot}$ during the total eclipse of March 29, 2006, in Turkey. This experiment by Kim et al.¹⁸ is another test case to check whether the ISCORE instrument with the polarization camera could replicate the 2-D distribution of the polarization angle from single images when it is deployed during the total solar eclipse of August 21, 2017, in United States.

5 Measuring the Electron Density Using the Polarization Camera

The original intent of the ISCORE instrument was to use the four filters to measure the electron temperature and speed whereas the required electron density for data analysis was to be obtained from the literature or models. However, with the advent of the polarization camera, even the electron density may be measured along with the electron temperature and speed measurements. By imaging the corona through an open filter, we can measure the total brightness, linearly polarized brightness, and unpolarized brightness in white light. This information is sufficient in determining the electron density profile in the solar corona. For example, November and Koutchmy¹⁹ used the 3.6-m Canada–France–Hawaii Telescope in Mauna Kea, Hawaii, to make white-light observations of the total solar eclipse of July 11, 1991, to determine the total brightness as a function of coronal height due to Thomson scattering. Here, the contribution due to the F-corona brightness was removed using a modeled profile of the F-coronal brightness and the K-coronal brightness was inverted to determine the electron density distribution with coronal height. Another example for measuring the electron density using the total and linearly polarized brightness in the region from $\sim(4-9) R_{\odot}$ from sun center using the “large angle and spectrometric coronagraph/white-light coronagraph” imaging from $(3.7-32) R_{\odot}$ (LASCO/C3) instrument on board the SOHO is explained by Gopalswamy and Yashiro.²⁰ The computational process to invert the K-coronal brightness to derive the electron density is described in detail in Baumbach²¹ and Shklovskii.²² Van de

Hulst²³ shows a technique employed to separate the K and F coronal brightness components from the total measured brightness and then to use the K-coronal brightness to derive the electron density. However, the task of deriving the electron density profile should be made much easier by using the equivalent of Figs. 19 and 20 of the solar corona produced by the polarization camera, where the camera would separately measure the K and F coronal brightness in the field of view of the ISCORE experiment. Then the K-coronal brightness could be used to derive the electron density profile in the solar corona and produce plots similar to Fig. 1 showing the K, F, and electron density profiles with coronal heights and could serve as a convincing test experiment to demonstrate the capability of the polarization camera.

6 Conclusion

We present two important capabilities that a polarization camera would render in measuring the linearly polarized brightness of the solar corona in the visible-light region of the solar spectrum using a solar coronagraph. First, this camera will eliminate the need to have a polarizer mechanism to turn a linear polarizer through at least three angles to obtain a linearly polarized brightness image, thus decreasing the overall weight, length, power requirements, and complexity of the instrument. Second, it will increase the temporal resolution.

Using the polarization camera to capture the images from the ISCORE experiment during a total solar eclipse will also allow us to measure the electron density from the white-light coronal images taken through an open filter, electron temperature from images taken through two filters centered at 385.0 and 410.0 nm, and electron speed from images taken through two filters centered at 398.7 and 423.3 in the low solar corona extending up to $4 R_{\odot}$ from the sun center. Although we failed to obtain any data in our very first attempt in conjunction with the total solar eclipse of March 9, 2016, in Maba, Indonesia, owing to rain and total cloud coverage, we intend to repeat the experiment in conjunction with the total eclipse of August 21, 2017, in the United States. Eventually, we plan to mount the ISCORE instrumental concept behind a ground or space coronagraph for synoptic observations for the three important physical parameters related to the coronal electrons.

Acknowledgments

The eclipse team to the total solar eclipse of March 9, 2016, thanks the Indonesian National Institute of Aeronautics and Space (LAPAN) for all the help rendered in transporting our equipment between Jakarta, Indonesia, and the eclipse observation site in Maba, Indonesia, in selecting an observing site and for providing all the other necessary logistics such as lodging and meals. We also thank the staff at the American Embassy in Indonesia for receiving and clearing customs of our eclipse equipment and for organizing public seminars to present our effort to the Indonesian audience. Nelson L. Reginald also acknowledges support from NASA grant CAN-NNG11PL10A2-Task125. Natchimuthuk Gopalswamy, PI of the eclipse task force, acknowledges the travel support provided by NASA HQ.

References

1. N. Gopalswamy, "Coronal mass ejections and space weather," in *Climate and Weather of the Sun-Earth System (CAWSES): Selected Papers from the 2007 Kyoto Symp.*, T. Tsuda et al., Eds., <http://www.terrapub.co.jp/onlineproceedings/ste/CAWSES2007/index.html> (2009).
2. D. E. Billings, *A Guide to the Solar Corona*, Academic Press, University of Michigan, New York (1966).
3. W. T. Thompson et al., "COR1 inner coronagraph for STEREO-SECCHI," *Proc. SPIE* **4853**, 1 (2003).
4. N. L. Reginald et al., "Electron-temperature maps of the low solar corona: ISCORE results from the total solar eclipse of 29 March 2006 in Libya," *Sol. Phys.* **260**, 347–361 (2009).
5. N. L. Reginald and J. M. Davila, "MACS for global measurement of the solar wind velocity and the thermal electron temperature during the total solar eclipse on 11 August 1999," *Sol. Phys.* **195**, 111–122 (2000).
6. N. L. Reginald et al., "Electron temperatures and flow speeds of the low solar corona: MACS results from the total solar eclipse of 29 March 2006 in Libya," *Sol. Phys.* **270**, 235–251 (2011).
7. K. J. H. Phillips, *Guide to the Sun*, Cambridge University Press, New York (1992).
8. I. Mann, "The solar f-corona—calculations of the optical and infrared brightness of circumsolar dust," *Astron. Astrophys.* **261**, 329–335 (1992).
9. D. Vorobiev and Z. Ninkov, "Compact polarimeters based on polarization—sensitive focal plane arrays," *Proc. SPIE* **9143**, 91435F (2014).
10. N. J. Brock, C. Crandall, and J. E. Miller, "Snap-shot imaging polarimeter: performance and applications," *Proc. SPIE* **9099**, 909903 (2014).
11. K. Serkowski, "Polarimeters for optical astronomy," in *Planets, Stars and Nebulae: Studied with Photopolarimetry*, T. Gehrels, Ed., p. 135, University of Arizona Press, Tucson, Arizona (1974).
12. N. N. Sytinskaya and V. V. Sharonov, "Measures of the brightness and color of the solar corona studied at six eclipses," in *Symp. Int. Astronomical Union*, p. 301 (1963).
13. C. E. Heiles, "Polarization of moon light," *Icarus* **2**, 350 (1963).
14. Y. Shkuratov et al., "Multispectral polarimetry as a tool to investigate texture and chemistry of lunar regolith particles," *Icarus* **187**, 406–416 (2007).
15. Y. Shkuratov et al., "Polarimetric mapping of the moon at the phase angle near polarization minimum," *Icarus* **198**, 1–6 (2008).
16. Y. Shkuratov et al., "Optical measurements of the moon as a tool to study its surface," *Planet. Space Sci.* **59**, 1326–1371 (2011).
17. A. Ferside, P. Masding, and C. Hooker, "Polarimetry of moonlight: a new method for determining the refractive index of the lunar regolith," *Icarus* **268**, 156–171 (2016).
18. I. S. Kim et al., "Imaging the structure of the low K-corona," *J. Geophys. Res.* (2016).
19. L. J. November and S. Koutchmy, "White-light coronal dark threads and density fine structure," *Astrophys. J.* **466**, 512–528 (1996).
20. N. Gopalswamy and S. Yashiro, "The strength and radial profile of the coronal magnetic field from the standoff distance of a coronal mass ejection-driven shock," *Astrophys. J. Lett.* **736**, L17–L21 (2011).
21. S. Baumbach, "Strahlung, ergiebigkeit und elektronendichte der sonnenkorona," *Astron. Nachr.* **263**, 121–134 (1937).
22. I. S. Shklovskii, *Physics of the Solar Corona*, Pergamon Press, University of California, Oxford, United Kingdom (1965).
23. H. C. Van de Hulst, "The electron density of the solar corona," *Bull. Astron. Inst. Netherlands.* **11**, 135 (1950).

Nelson L. Reginald received his BSc degree in physics and pure mathematics from the University of Peradeniya, Sri Lanka, and his MS and PhD degrees in physics from the University of Delaware, USA, and his management accountant degree from the Chartered Institute of Management Accountants, UK. He is a research astrophysicist and has conducted ground experiments during total solar eclipses to study the low solar corona close to the solar limb, which is possible only during total solar eclipses.

Natchimuthuk Gopalswamy is an astrophysicist at NASA's Goddard Space Flight Center, Solar Physics Laboratory. His research is in the area of solar and solar terrestrial physics including coronal mass ejections, solar flares, solar energetic particles, solar radio bursts, interplanetary shocks, and space weather. He is also involved in coronagraphy and radio astronomy. He is a coinvestigator of the Solar Terrestrial Relations Observatory (STEREO) Mission and the director of the Coordinated Data Analysis Workshop Data Center.

Biographies for the other authors are not available.